Thermal conductivities of solid and molten silicates: Implications for dynamos in mercury-like proto-planets

D. Freitas, J. Monteux, Denis Andrault, Geeth Manthilake, A. Mathieu, Federica Schiavi, N. Cluzel

Thermal conductivities of solid and molten silicates: implications for dynamos in Mercury-like proto-planets

D. Freitas[1,$]*, J. Monteux[1], D. Andrault[1], G. Manthilake[1], A. Mathieu[1], F. Schiavi[1], N. Cluzel[1]

[1]Université Clermont Auvergne, CNRS, IRD, OPGC, Laboratoire Magmas et Volcans, F-6300 Clermont-Ferrand, France
[$]Now at School of Geosciences, Grant Institute, The King's Buildings, The University of Edinburgh, West Mains Road, Edinburgh EH9 3JW, United Kingdom

*Corresponding Author: Damien Freitas (damien.freitas@ed.ac.uk)

Abstract

Remanent magnetization and active magnetic fields have been detected for several telluric planetary bodies in the solar system (Earth, Mercury, Moon, Mars) suggesting the presence of core dynamos active at the early stages of the planet formation and variable lifetimes. Among the factors controlling the possibility of core dynamos generation, the dynamics of the surrounding silicate mantle and its associated thermal properties are crucial. The mantle governs the heat evacuation from the core and as a consequence the likeliness of an early thermally driven dynamo. In the case of planets with a thick mantle (associated with supercritical Rayleigh numbers), the core heat is efficiently removed by mantle convection and early thermally-driven dynamos are likely. At the opposite, planets with a thin mantle (associated with subcritical Rayleigh numbers) might evacuate their inner heat by diffusion only, making early thermally-driven dynamos difficult. Within the Solar System, Mercury is a potential example of such a regime. Its small mantle thickness over the planet radius ratio might be inherent to its small orbital semi-axis and hence, might be ubiquitous among the terrestrial objects formed close to their star.

To constrain the likeliness of a thermally driven dynamo on "Mercury-like" planets (i.e. with large Rc/R), we present new thermal diffusivity measurements of various solid, glassy and molten samples. We applied the Angstrom method on cylindrical samples during multi-anvil apparatus experiments at pressures of 2 GPa and temperatures up to 1700 K. Thermal diffusivities and conductivities were estimated for solid and partially molten peridotites, with various melt fractions, and for basaltic and rhyolitic glasses and melts. Our study demonstrates that melts have similar thermal properties despite a broad range of composition investigated. The melts reveal much lower thermal conductivities than the solids with almost an order of magnitude of decrease: 1.70 (±0.19) to 2.29 (±0.26) W/m/K against 0.18 (±0.01) to 0.41 (±0.03) W/m/K for peridotites at high temperatures and various melts respectively. Partially molten samples lie in between and several predictive laws are proposed as a function of the melt fraction and solid/melt texture.

Using our results into forward calculations of heat fluxes for dynamo generation for Mercury-like planets, we quantify the effect of mantle melting on the occurrence of thermally driven dynamos. The presence of a mushy mantle and partial melting could significantly reduce the ability of the mantle to evacuate the heat from the core and can prevent, shut or affect the presence of a planetary magnetic field. The buoyancy and fate of molten material in such bodies can thus influence the magnetic history of the planet. Future observations of Mercury-like planets accreted near their star and the detections of their magnetic signatures could provide constraints on their inner state and partial melting histories.

Introduction

The presence of internally generated magnetic fields is a variable feature among telluric bodies in the inner solar system. While few are currently active, such as for Mercury and Earth, several are now extinct, as observed for the Moon, Venus and Mars. On terrestrial planets currently exhibiting a dynamo, the generated magnetic fields characteristics are very different. Earth's magnetic field is very intense 25-65 µT, originating from the core and present for at least 3.5 Ga (Tarduno et al. 2010). Mercury's field strength is much weaker, representing around a 1% of Earth's one (Kabin et al. 2008; Anderson et al., 2011) and its shape is also unique among the different detection in the solar system (Tian et al., 2015). According to the remnant magnetization measured in the crust, it was proposed that such weak magnetic activity occurred during the last 3.9 Ga (Johnson et al. 2015). The source of such a weak-and-prolonged dynamo is still largely debated (Manthilake et al. 2019). In the meantime, there are several evidences for an intrinsic dynamo during the early stages of both Mars and Moon (Acuña et al., 1999; Hood et al., 2010). Their dynamo seems to cease around 4.1-3.9 Ga ago for Mars (Johnson and Phillips, 2005; Lillis et al., 2008, Lillis et al., 2013) and exhibits a somewhat complicated history for the Moon with a strong dynamo between 4.25 and 3.5 Ga, followed by a weak persistence up to 2.5-2 Ga ago (Tikoo et al. 2014, Lawrence et al. 2008, Garrick-Bethell et al., 2009, Mighani et al. 2020). For Venus, the early presence of a dynamo remains yet unconstrained but may be detectable in future explorations (Nimmo et al. 2002; O'Rourke et al. 2019). More broadly, evidences of paleomagnetic anomalies indicate that the angrite parent bodies, originating from inner regions of the solar system, were subject to an early internally generated dynamo (Weiss et al. 2008). All these elements suggest that transient dynamos might be a somewhat common feature in telluric bodies (Monteux et al. 2011).

The presence of early dynamos is highly conditioned by the internal structure of the planet and its capacity to release the heat accumulated during the accretion processes (accretion, metal/silicate differentiation, core and mantle crystallization) as well as short-lived radiogenic heating. As heat conduction is an inefficient heat transport process in silicates at high temperatures (Hofmeister and Branlund, 2015), the onset of a mantle global convection is a crucial step in planet's thermal history. Convection starts when the Rayleigh number (Ra) of the terrestrial mantle is larger than the critical Rayleigh number (Ra_c). The higher is Ra, the stronger the convection, and the more efficient the heat transport. In contrast, heat is only transported by conduction for a terrestrial mantle with a $Ra<Ra_c$. As Ra scales with mantle thickness (h_{mantle}) as h_{mantle}^3, convection should take place easily in planets with a thick silicate mantle, even after the solidification of the early magma ocean stage. Consequences are efficient evacuation of the inner heat and the possible occurrence of a dynamo. At the opposite, bodies with a thinner mantle lead to smaller Ra values, making convection unlikely and dynamos more difficult to generate.

Mercury is the most interesting planet for our study. Indeed, its mantle is thin 420 ± 30 km (Hauck et al. 2013) and its core occupies almost 55% of planet's volume and 65% of the planet mass (Strom and Spague, 2003; Charlier and Namur, 2019). Hence, the mantle of Mercury is controversially at the limit between conductive and convective regimes (Breuer et al. 2007). Different scenarios could

101 explain the small h_{mantle}/planet radius (R) ratio on Mercury (Charlier and Namur, 2019): (1) primordial
102 nebular processes, yielding to the enrichment of metal over silicate materials in the inner solar system
103 (Ebel and Grossman, 2000; Wurm et al. 2013; Weidenschilling 1978), (2) highly energetic accretional
104 collisions inducing a major loss of the silicate fraction (Benz et al. 1988, Asphaug and Reufer, 2014),
105 and (3) post–accretion scenarios, with major vaporization of the volatile and silicate elements from
106 the planet during magma ocean stage (Fegley and Cameron 1987; Boujibar et al., 2015). If scenarios
107 (1) and (3) are dominant, then "Mercury-like" planets with small h_{mantle}/R ratio would be ubiquitous
108 within all planetary systems. Moreover, such a small ratio would be prevailing during the whole
109 accretionary processes. Mercury-like bodies could adopt a wide range of possible compositions
110 depending on their history. For example, bodies accreted from reduced enstatite and/or carbonaceous
111 bencubbinite chondrites (Malavergne et al. 2010) could present a mantle composition similar to
112 terrestrial lherzolite, but with a sulfur content potentially as high as 11 wt.% (Namur et al. 2016).
113 Accordingly, the diversity of the silicate samples found on Earth in the forms of rocks, melts and
114 glasses is a good proxy to decipher the properties of a range of mantle-relevant silicate compositions
115 on Mercury-like bodies. Depending on the planet size and the h_{mantle}/R ratio, the internal pressure
116 ranges from a few MPa to several GPa. We note that extensive mantle melting likely occurred at
117 different stages of the history of such Mercury-like bodies. Major energy incomes are expected from
118 the vicinity to the young Sun (2500 to 3500 K according Charlier and Namur, 2019), internal energy
119 release (chemical and gravitational differentiation, core crystallization), and presence of short-period
120 radioactive elements (Al^{26}, K^{40} etc.). The very high temperatures likely induce extensive melting of
121 the thin mantle up to the core-mantle boundary (CMB).

122   As mentioned above, dynamo generation could be difficult for Mercury-like planets, due to the
123 subcritical value of Ra possibly disabling mantle convection. In such case, heat transfer by conduction
124 would dominate the planet history and the thermal conductivity of the silicate mantle is a key
125 parameter governing the early core heat flow. Silicates thermal conduction properties are now well
126 characterized at ambient conditions (Hofmeister and Branlund, 2015). Among them, the most
127 common geological minerals were characterized in the forms of single crystal and polycrystalline
128 aggregates: olivine (Osako et al. 2004; Xu et al. 2004; Perterman and Hofmeister 2006; Gibert et al.
129 2005), periclase (Hofmeister and Branlund, 2015), feldspar (Pertermann et al. 2008; Hofmeister et al.
130 2009; Branlund and Hofmeister, 2012) and pyroxenes (Hofmeister 2012, Hofmeister and Pertermann
131 2008) as well as peridotite rocks (Gibert et al. 2005; Beck 1978), which have been extensively studied
132 due to their important geological implications. The thermal diffusivities of minerals are linked to the
133 characteristics of their lattice structure and modes of phonon generation and propagation as a function
134 of temperature. For silicates, lattice thermal diffusivities usually decrease with increasing temperature
135 following a 1/T dependence. At the opposite, the diffusivities increase while increasing pressure,
136 however, the temperature dependence is much greater than that of pressure over the considered ranges
137 for small planets. The resulting implication is that mantle rocks and minerals are poor thermal
138 conductors in planetary interiors. Recent measurements of thermal diffusivities of glasses and melts
139 at ambient pressure suggested that the non-crystalline silicates are even more insulating than the
140 minerals (Hofmeister et al. 2009, 2014, Romine et al. 2012).

141   Measurements of thermal diffusivities at relevant conditions of planetary mantles encompass
142 important difficulties, which were overcome by the use of different techniques (see Hofmeister and
143 Brandlund 2015 for a critical review). Measurements were reported over a wide P and T range for
144 large volume samples of olivine, periclase, bridgmanite using Angström or Pulse method in solid
145 pressure apparatus (Osako et al. 2004; Xu et al. 2004; Manthilake et al. 2011a and 2011b, Zhang et
146 al. 2019). Up to now, accurate measurements of geologically relevant silicate glass, partially molten
147 systems and melts at planetary interior conditions remain scarce if not absent. The available results
148 report a nearly flat evolution of thermal diffusivities with the temperature above 1000 K for silicates,
149 glass and melts (Hofmeister et al. 2014; Hofmeister and Banlund, 2015), suggesting that the

measurements above the melting temperature could be safely extrapolated to planetary P-T conditions.

In this study, we aim at better constraining the thermal properties of Mercury–like protoplanets where convection is unlikely and heat is mostly removed by diffusion. We perform HP-HT *in situ* thermal diffusivities measurements of solid, partially molten and fully molten silicate for various compositions in Multi-anvil apparatus and using Angström method. Then, we constrain the likeliness of a thermally driven dynamo during the early stages of the evolution of a Mercury-like planet. We consider a wide range of planet sizes ($1 \text{ km} < R < R_{Mercury}$) and thermal states (with solid and partially molten mantles) on the dynamo likeliness.

Experimental and analytical methods

High-pressure assemblies:

High-pressure and high-temperature experiments were performed using a 1500-ton Kawai type Multi-anvil apparatus. All experiments were conducted at 2 GPa, based on a previous press-load vs sample pressure calibration (Boujibar et al. 2014), providing an uncertainty of ~0.1 GPa at pressures <5 GPa. We used octahedral pressure media with full length edges composed of MgO doped with Cr_2O_3 (5 wt. %) in a 25/17 multi-anvil configuration (octahedron edge length / anvil truncation edge length) (Figure 1). Our assembly was designed to accommodate the specific requirements for measurements of thermal conductivity of relatively large samples (4 mm long for 4-3.5 mm diameter). All ceramic parts of the cell assembly, including the pressure media, were fired at 1373 K prior assembling in order to remove the absorbed moisture. Oxygen fugacity of the sample was not controlled during the experiments but is expected to be quite reducing due to the presence of the graphite furnace. The use of a steeped graphite furnace helped reducing thermal gradients. Thermal loss from the sample zone was further reduced by the use of a thick zirconia (ZrO_2) sleeve around the furnace. Thermal gradients in our assembly were computed using the software developed by Hernlund et al. 2006. The models show temperature gradients within the sample volume limited to ~7.5 K/mm vertically and even less radially/horizontally (Figure S1). On the other hand, uncertainties of our thermocouple reading (i.e. where the conductivity measurement is performed, see below) are less than 5 K on absolute and 0.1 K in relative temperatures.

Previous experimental studies described the difficulties to perform a good measurement of thermal diffusivity for a molten sample, due to a potential sample deformation (Hofmeister et al. 2009, 2014; Romine et al. 2012). However, deformation remained minor in our experiments, as evidenced by the good reproducibility of the measurements during the repeated cycles of heating and cooling (Figures 1 and 2) as well as the shape of the recovered samples (Figures S6, S7 and S8).

Two tungsten-rhenium ($W_{95}Re_5$-$W_{74}Re_{26}$) thermocouples of 75 µm of diameter were used to measure temperature oscillations at the center (in 300 and 600 µm drilled holes in solids and glasses, respectively) and at the edge of the cylindrical sample. Special care was given to ensure that the junction points of the two thermocouples were located in the same sample plane perpendicular to the cylinder axis. Measurements of the thermal conductivity of melts and glasses have always been particularly challenging due to the risk of thermocouple short circuit, because melts, even dry, are good electrical conductors (Tyburczy and Waff, 1983; Ni et al. 2011). To prevent this effect, thermocouples were inserted in alumina tubes of 0.6 mm diameter and 170 µm wall thickness. While these tubes show good resistance to cold compression and almost no reaction with the samples, even at very high temperature, some leakages for low viscosity basaltic melts have been identified. Their occurrence was taken in account for thermal diffusivity estimations (see Supplementary Text S1 and Figures S2 and S3).

200 Angström method for thermal diffusivity measurements

201 We aim at determining thermal diffusivities of geological samples such as peridotites, mafic and
202 felsic glasses and their melts at high pressure and high temperature using a double contact method:
203 the Angström method. Experimental configurations, assemblies and data treatment are similar to
204 several previous studies (Fujisawa et al. 1968; Kanamori et al. 1969; Katsura 1993; Xu et al. 2004;
205 Manthilake et al. 2011a and 2011b). Briefly, a temperature wave is generated radially in a cylindrical
206 sample by the surrounding heater sleeve of the multi-anvil assembly (Figure 1). Oscillations are
207 generated with controlled frequency and period by modulating the power supply. Periodic
208 temperature signals are recorded by two thermocouples fixed in the center and on the edge of the
209 sample cylinder. At frequencies higher than 1.5 Hz, the signal can get noisier due to a limited time
210 resolution of the recording system.

211 The recorded signals, for each thermocouple channel, are fitted by a nonlinear least square solver
212 (lsqcurvefit on Matlab© using Levenberg-Marquardt algorithm):

$$213 \quad \Delta T = A_0 + A_1 t + A_2 \sin\left(2\pi A_3 t + \frac{A_4 \pi}{180}\right) \quad (1)$$

214 Following this method, we obtained the amplitude of the temperature variation (A_2), frequency
215 (A_3), and phase (A_4) of the recorded wave as a function of time (t), for the two thermocouples. Errors
216 are quantified based on the residue on the non-linear curve fitting (the *nlparci* function in Matlab©).
217 To infer thermal diffusivity or conductivity from these parameters, the equation of conductive heat
218 transport has to be solved. Here we consider the sample as an infinite uniform cylinder and assume
219 that the heat flow is negligible in the vertical direction, thanks to a relatively long cylindrical heater.
220 The following equation, expressed in cylindrical coordinates by Carlsaw and Jaegger (1959), has to
221 be inverted in order to retrieve the diffusivity of the sample:

$$222 \quad \frac{dT}{dt} = D\left(\frac{d^2 T}{dr^2} + \frac{1}{r}\frac{dT}{dr}\right) \quad (2)$$

223 where r is the radial distance from the axis, T the temperature, t the time, and D the thermal diffusivity.
224 The boundary condition of our setup is:

$$225 \quad \frac{dT}{dr} = 0, at\ r = 0 \quad (3)$$

226 If we consider harmonic excitation at a distance $r = R$ from the axis in normal or complex form:

$$227 \quad T_R = B_0 + B_1 \cos wt \ \leftrightarrow \ T_R = b_0 + b_1 \operatorname{Re}(\exp iwt) \quad (4)$$

228 where B_0, B_1, b_0 and b_1 are constants and Re is the real part of the exponential. The solution of the
229 radial flow equation with the boundary conditions developed above can be expressed as:

$$230 \quad T_R = b_0 + b_1 \left| J_0(\sqrt{-i} * x) * \frac{\exp(iwt)}{J_0(\sqrt{-i} * l)} \right| \quad (5)$$

231 where:

$$232 \quad l = (^W/_K)^{1/2} R \ and \ x = (^W/_K)^{1/2} r \quad (6)$$

233 for $0 \leq r \leq R$, where w is the angular frequency and J_0 is the Bessel function of the first kind (integer
234 order $n = 0$). At $r = 0$ and $r = R$ we have:

$$235 \quad T_0 = b_0 + b_1 \theta \cos(wt - \varphi) \quad (7)$$
$$236 \quad T_R = b_0 + b_1 \cos wt \quad (8)$$

237 where:

$$238 \quad \theta = \frac{1}{\sqrt{bei(u)^2 + ber(u)^2}} \quad (9)$$

$$239 \quad \varphi = \tan^{-1}\left(\frac{bei(u)}{ber(u)}\right) \quad (10)$$

240 where θ is the amplitude ratio and φ the phase shift between the two harmonic temperature
241 measurements and *bei* and *ber* are imaginary and real parts of the Bessel function of the first kind,
242 respectively. The solution to the eq. (4) can be written using the dimensionless argument u, from

5

243 which thermal diffusivity (*D*) can be directly estimated knowing angular frequency (*w*) and sample
244 radius (*d*).

$$u = d(w/D)^{1/2} \ (11)$$

246   Thanks to the Eqs.9, 10, and 11, the diffusivity was then retrieved via forward Monte Carlo
247 simulation and neighborhood algorithm (Sambridge, 2002). In this step, different values of
248 diffusivities are generated and theoretical phase shifts and amplitude ratios are calculated. These
249 values are compared to the values measured in our experiments. When the differences between the
250 computed solution and the experimental determination tend to 0 (minimization step), the correct
251 diffusivity is then obtained if the sample radius (d) and angular frequency (w) are known. We note
252 that mathematical solutions appear every 360° for the phase shift. Such erroneous solutions are
253 checked manually and discarded.
254   For most of our experiments, we observe a significant variation of the refined raw-diffusivity
255 value as a function of the heat-source frequency. This effect was already reported in the literature.
256 Different equations were proposed to refine a real value of diffusivity, corresponding to the infinite
257 frequency asymptote, based on non-linear equations. While Manthilake et al. (2011b) used:

$$D = D_\infty + A_0 \, exp(A_1 * f) \ (12)$$

259 Xu et al. (2004) used:

$$D = D_\infty + A_0 exp\left(\frac{-f}{f_0}\right) (13)$$

261 where *D* is diffusivity, *f* source frequency, f_0 asymptote frequency and A_0 and A_1 constants. In these
262 equations, D_∞, A_n and f_0 are inverted parameters. For a better fit of our experimental data and to
263 minimize the uncertainties on the parameters, we adopt Eq. 13. On the other hand, for experiments
264 presenting no systematic dependence of the raw-diffusivity with frequency, we consider as real value
265 the average value between the raw-diffusivity values measured at all frequencies (Xu et al. 2004;
266 Manthilake et al. 2011b).

268 <u>Experimental uncertainties</u>
269   Experimental measurements of thermal diffusivities and their further transformation into
270 thermal conductivities generate uncertainties originating from the estimations of pressure,
271 temperature, sample dimensions and the data fitting itself. Experimental uncertainties on pressure and
272 temperature are presented above (~0.1 GPa and ~5 K, respectively). Sample lengths prior to the
273 sample loading (d_0) and after the melting experiments were determined with a high precision digital
274 gauge (accuracy of ~1 µm) and using the Scanning Electron Microscope (FEG-SEM), respectively
275 (see Table 1). Then, the sample radius during the experiment at high pressure and temperature was
276 calculated using:

$$d(P,T) = d_0 * \left(1 - \alpha(T - 298) + \frac{P}{K}\right)^{-1/3} (14)$$

278 where α is the thermal expansion and *K* the bulk modulus of the sample. For these calculations only
279 samples radii before experiments were considered, as post mortem measurements are affected by
280 decompression cracks (highlighted by the larger values measured after the experiments in Table 1).
281 Moreover, the distance between the two thermocouples could not be measured precisely for a few
282 samples. The values of all experimental parameters are provided in Supplementary Materials (Text
283 S4 and Figure S4). Altogether, final uncertainty on the sample length is between 5 and 10 µm.
284   There are other uncertainties associated with the procedure of data fitting for the determination
285 of raw thermal diffusivities. Experimental phase shifts and amplitude ratios (Eqs. 9 and 10) are
286 determined with a precision generally better than 1% and majored by 3% in the worst cases. In the
287 course of the Monte Carlo simulation, the differences between experimental and theoretical
288 diffusivities are recorded and used a posteriori to refine uncertainties within 1σ errors.
289   Then, real thermal diffusivities are refined from the raw-diffusivities using either (i) the
290 asymptotic non-linear fit for experiments presenting a dependence in frequency (Eq. 13, which yields

6

important uncertainties on the refined parameters) or by averaging (see Methods). The error on average (σ_{AVG}) is:

$$\sigma_{AVG} = \sqrt{\left(\frac{1}{n}\right)^2 * \sum_{1:n} \sigma_D^2} \quad (15)$$

where n is the number of diffusivity measurements performed at different frequencies and σ_D is the error on each diffusivity. Raw diffusivities recovered from Monte Carlo processing have errors of ~1%, similar to those of phase shift and amplitude ratio. If the fitting step is realized with Eq. 13, errors of raw data are used as weights in the inversion. The standard deviations are usually between 1 and 10% of the real asymptotic diffusivity. If the averaging method is selected, the standard deviation, estimated via Eq. 15, is usually about 1% of the final value.

A final source of uncertainties come from other technical issues and apparatus reproducibility, which are inherent to such challenging experiments. We considered that final error must be majored by 5 % of the value. The relative uncertainties become even higher after conversion into thermal conductivities due to uncertainties and simplifications on the sample density and heat capacity at high pressure and temperature (see Supplementary Text S4).

Experimental procedure:

We performed a suite of three heating and cooling cycles to provide an important number of data and maximize the quality of recovered data. A first cycle was run up to 500 °C for moisture removal by 50°C steps (Figure. 2). The second cycle was run up to glass transition temperature (Tg) by 100°C steps. Tg varies according to rock composition and its water content (Giordano et al., 2005). For our dry samples, the temperature of 800°C happened to be above Tg for all our compositions. The temperature was then decreased down to 150°C by 100°C steps. The quality of the measurement is usually better during the cooling cycle once (1) the sample has thermally equilibrated with the assembly, (2) moisture has been removed, and (3) a better contact was achieved between the sample and the thermocouples due to local flow in the solid-state. The redistribution of matter under high temperature cancels most of the potential artifacts associated with the presence of pores/voids between the sample and the thermocouples (Hofmeister et al. 2009). Hence, data recorded during the last cycles were considered for final values.

In the last cycle, we heated the sample up to its melting temperature by 100°C steps or 50°C near the melting point. The sample was maintained above its melting point for less than 1 hour, to avoid sample leakage and chemical reaction with the surrounding parts. The sample was then quenched to 600-550°C. This step produces a glassy sample from which measurements at low temperature are performed.

Temperature oscillations of the two thermocouples were measured at each temperature step for both heating and cooling cycles, at 12 different oscillating frequencies between 0.1 and 1.5 Hz. The measurements were performed after at least 2 min of thermal equilibration to reach a stable regime (the smaller is the frequency, the longer is the required equilibration time). Then, the recording duration was 1 to 2 minutes or at least 10 oscillating periods. The measurement at the 12 frequencies took between 20 to 30 minutes. Thus, the duration of each experiment was more than 12 hours.

Chemical and textural analyses:

Recovered samples were cut parallel and perpendicular to the cylindrical furnace and each section was polished with great care. We could observe the position of the two thermocouples junctions, measure the sample radius and perform the textural and chemical analyses (see Supplementary Figures S6, S7, and S8).

Micro-textures were observed with a Scanning Electron Microscope (SEM) JEOL Jeol JSM-5910 LV using an accelerating voltage of 15 kV and a working distance of 11.4 mm. The 2D phase proportions of our partially molten peridotite samples were obtained from the analyses of qualitative

chemical maps obtained by energy-dispersive X-ray spectroscopy (EDX) in the SEM. The images were binarized and phases were individually separated allowing textural analyses with the FOAMS software (Shea et al., 2010). A more detailed description is given in Freitas et al. (2019). On the other hand, quantitative chemical analyses were performed on both our starting materials and experiment products using the electron probe micro analyzer (EPMA). Chemical and textural analyses of starting materials are reported in the Supplementary Text S2, Figures S6 to S13 and Tables S1, S2, S3 and S4. Analyses of recovered runs are detailed in Supplementary Text S3, supplementary Figures S6 to S7 and Tables S1, S2, S3 and S4.

Water contents were estimated using the ICP-AES for the peridotite starting materials and via Raman spectroscopy for the recovered samples. Raman spectra were collected with a Renishaw InVia confocal Raman micro spectrometer, equipped with a 532 nm diode laser and a Leica DM 2500M optical microscope. Measurements were carried out using a 2400 grooves/mm grating, a 100× microscope objective, a slit aperture set to either 20 µm or 65 µm and a laser power of 8 mW for glasses and 16 or 75 mW for olivine. The resulting lateral and axial resolutions were of ~1 and 3 μm, respectively, and the spectral resolution was better than 1 cm^{-1}. Daily calibration of the spectrometer was performed based on the 520.5 cm^{-1} peak of Si. Spectra were recorded from ~100 to 1300 cm^{-1} (alumino-silicate network domain) and from ~3000 to 3800 cm^{-1} (water domain), with variable acquisition times ranging between 5 and 120 s for silicate bands and 120 and 240 s for water domain depending on the water content (Figures S11 to S17). For water quantification in olivine and glass, we followed the procedures reported by Bolfan-Casanova et al. (2014) and Schiavi et al. (2018). We used both (1) the external calibration procedure, which is based on a set of hydrous olivine standards from (Bolfan-Casanova et al. 2014) and different types of silicate glasses ranging from basaltic to rhyolitic compositions (Schiavi et al., 2018; Médard and Grove, 2008), and (2) the internal calibration procedure, based on the correlation between the water concentration in olivine or glass and the relative areas of the water and silicate Raman bands (OH/Si integrated intensity ratio). The discrepancy between the two methods is small. Water contents in the standard materials were previously determined using the FTIR technique.

Results

We performed a total of 11 thermal diffusivity experiments on various chemical compositions, using the Angström method (details in Table 1). In this section, we first describe phase shifts and amplitude ratios between the two thermocouples and their conversion into thermal diffusivities and conductivities. We detail the post-mortem chemical and textural analyses in the Supplementary Text S3, Tables S1 to S4 and Figures S6 to S13.

Phase shift, amplitude ratio and the refined raw-thermal diffusivities

Signals recorded during the experiments are sinusoidal oscillations with varying frequencies. The thermocouple located at the sample center (labeled TC1 in Figure 3) presents a phase delay and a smaller amplitude compared to the thermocouple located at the sample edge (labeled TC2 in Figure 3). Typical raw signals and their fits are presented in Figure 3, while the refined (absolute) phase shifts and amplitude ratio are reported in Figure 4. Both the magnitude of phase shift and amplitude ratio change significantly with the type of sample and the experimental conditions, including the source frequency. At a constant frequency, the phase shift increases with increasing temperature. At a constant temperature, the phase shift increases with increasing the excitation frequency. The amplitude ratio is decreasing with increasing frequency and temperature.

Globally, the refined thermal diffusivities present a comparable evolution of temperature at all signal frequencies (see an example in Figure 5). When the frequency dependence is larger than the experimental uncertainty (Figure 6), we use Eq. 13 to refine the true asymptotic value of the thermal conductivity. Alternatively, when the temperature dependence is below the experimental uncertainty

389 or when no clear frequency trends is visible, we average the different raw-diffusivity values (see
390 Methods). In the wide majority of the cases, diffusivity values inferred from phase shifts appear to be
391 more robust and with a lesser degree of uncertainty, compared to values inferred from difference of
392 amplitude, in agreement with previous studies (Kanamori et al. 1969 and Xu et al. 2004). Hence,
393 despite similar values obtained with the two methods, values refined from phase shift were preferred.
394

395 *Results for peridotite*
396   For peridotite, our two successful experiments present a smooth evolution with temperature,
397 yielding diffusivities values decreasing from $1.7(\pm0.1)e^{-6}$ to $7.5(\pm0.4)e^{-7}$ m²/s for sample M804 and
398 $1.5(\pm0.8)e^{-6}$ to $5.5e^{-7}$ m²/s for sample M847 (Figure 6a), with an uncertainty of about 5 to 10% for
399 each sample. We attribute the relative discrepancy to a difference of sample mineralogy between the
400 two samples, due to the coarse grain size of the core drilled peridotite (see Supplementary Texts S2
401 and S3 and Figures S8 and S9). Olivine has a higher intrinsic thermal diffusivity than the other phases
402 present in peridotite such as pyroxenes and spinel (Hofmeister and Branlund, 2015). M804 may
403 contain more olivine, inducing higher diffusivities than M847. In this respect, the results for two
404 samples are thus compatible with each other and the differences are representative of the variability
405 of thermal diffusivity that can be expected among the compositional variability of peridotites (from
406 lherzolites to dunites).
407   Thermal diffusivities of our peridotite samples scale as a function of ~1/T, as expected from the
408 standard equation provided by Hofmeister and Branlund, 2015:
409 $$D_{lat} = a * T^{-b} + c * T \quad (16)$$
410 where *T* is the temperature (K), and *a*, *b* and *c* are adjustable parameters (Table 2). The quality of the
411 fit is excellent up to a temperature of ~1300 K corresponding to the onset of peridotite melting. We
412 therefore exclude the data points above 1300 K to model the thermal properties of solid peridotite.
413

414 *Results for basalts*
415   For our basaltic samples, the measured diffusivities plot over a broad range of values, from
416 $1.0(\pm0.1)e^{-6}$ to $3.0(\pm0.2)e^{-7}$ m²/s (Figure 6b), with an uncertainty of ~5% for each experiment. The
417 discrepancy is particularly important at low temperatures. Also, a same sample yields thermal
418 diffusivity values significantly different along the different cycles of the experimental procedure
419 (between C2, H3 and the final quench, see Figure S5). Samples with the highest diffusivities at low
420 temperatures present a rapid decrease of diffusivity with increasing temperature. On the other hand,
421 samples with the lowest diffusivities show very small temperature dependence. It yields to a
422 convergence of all diffusivity measurements at ~1000 K. Based on a study of rhyolitic glasses,
423 Romine et al. (2012) reported a moderate temperature dependence, similar to our samples presenting
424 a low diffusivity, and an increase of 0.0192 mm²/s of the glass diffusivity per percent of crystallinity.
425 For our starting materials with less than 5 vol.% of crystals (see Supplementary Text S2 and S3,
426 Figure S7), the effect of microlites could account for ~0.1 mm²/s of variation in our diffusivity values,
427 which correspond to less than ~10% of observed differences. However, the presence of 35 vol.% of
428 crystals in the recovered sample M807 would explain not only its high thermal diffusivity at low
429 temperature, but also its strong temperature dependence that is typical of crystals (see Beck et al.,
430 1978; Romine et al. 2012; Hofmeister and Branlund 2015 and our peridotite trends in Figure 6a). The
431 recrystallization of M807 is not surprising, since the second cycle of annealing was performed above
432 its Tg (Figures 2 and S5). The crystallinity of other samples depends on the applied cycles of
433 annealing at a temperature eventually close to their Tg. Nonetheless, diffusivities of all samples
434 converge at increasing temperatures, because the conductivity of crystals is not much greater than
435 that of the glass at high temperature, especially if microlites are low diffusivity silicates such as
436 pyroxenes, plagioclase or spinels (see Hofmeister and Branlund 2015 for mineral diffusivity
437 compilations). Over the 5 basaltic samples investigated in this study, the diffusivity trends indicate
438 either significant recrystallization of M807 (DR07-MORB) and M662 (EPR-MORB), or negligible

439 crystallization of M844 and M846 (DR11-MORB) and M836 (synthetic haplobasalt). The sample
440 crystallization is likely to evolve during the thermal diffusivity measurements in step H3 (up to
441 melting point) of the experiments performed at a temperature significantly above the Tg. For this
442 reason, the crystallinity determined on the recovered samples is only a qualitative measurement of
443 the sample properties at high temperatures.
444
445 *Results for rhyolites*
446   Measured diffusivities of rhyolite samples also plot over a broad range of values from $1.4(\pm0.8)e^{-6}$
447 to $4.0(\pm0.2)e^{-7}$ m²/s, with an uncertainty of about 5% for each experiment (Figure 6c). The
448 discrepancy appears similar than for the basalt samples, as the sample presenting higher diffusivities
449 also show a major temperature dependence at low temperature. The presence of less than 2 vol.% of
450 crystals in the starting material could account for a diffusivity increase of 0.038 mm²/s at maximum
451 (Romine et al., 2012). Still, the diffusivity trends suggest a major recrystallization at high-temperature
452 for M808 (Güney Dag) and M843 (ATHO), some crystallization for M843 (ATHO), and negligible
453 crystallization for M850 (Güney Dag).
454
455 *Properties of melts and partially molten samples*
456   In addition to the evolutions described above, a strong decrease of the thermal diffusivity is
457 observed for most of our samples at the highest temperatures (Figure 6). The decrease occurs at
458 temperatures around 1300 K for peridotites, 1200 K for basalts and >1050 K for rhyolites. Such
459 temperatures are in agreement with the melting or glass transition temperatures, depending if the
460 sample is a peridotite or a glass, recrystallized or not. Similar changes were already reported at
461 temperatures above the glass transition (Hofmeister 2009, 2014, Romine et al. 2012).
462   The amplitude of the decrease is 45-50% in peridotites, which recovered samples present a degree
463 of partial melting (F) up to 23%, 35-70% for basalts and <30% for rhyolites samples. The more
464 pronounced decrease in molten peridotites is probably due to a more contrasted change of the local
465 structure at the melting point, between the minerals and the melt (see discussion). On the other hand,
466 the minor change of diffusivity for rhyolites at Tg could be related to their high SiO_2-content, which
467 preserves a polymerized structure in the melt above the glass transition.
468
469 Thermal conductivities
470   Thermal conductivities (κ) can then be computed from thermal diffusivities following:
471 $$\kappa (P,T) = D(P,T) * \rho(P,T) * C_P(P,T) \ (17)$$
472 where $\rho(P,T)$ and $C_P(P,T)$ are the sample density and heat capacity, respectively. For our calculations,
473 we considered ρ and Cp values in standard conditions when the P and/or T dependences were not
474 available in the literature (see Supplementary Text S4 and Figure S4).
475   Conductivities calculated for peridotites evolve from 4.32 (±0.48) to 1.70 (±0.19) W/m/K with
476 increasing the temperature up to the melting point. Values for basalts range from 1.7 ($\pm8.0e^{-2}$) to 0.5
477 ($\pm4.0e^{-2}$) W/m/K, whereas those for rhyolite lie between 1.1 ($\pm9.0e^{-2}$) and 0.3 ($\pm3.0e^{-2}$) W/m/K for
478 low to high temperatures, respectively. At the melting temperature, our partially molten peridotites
479 display values of 1.19 (±0.16) to 0.93 (±0.10) W/m/K, whereas melts present relatively lower values
480 of 0.34 (±0.2) to 0.18 (±0.1) W/m/K for basaltic and 0.41 (±0.3) to 0.31 (±0.3) for rhyolitic
481 compositions (See Figure 7 and Table 3). We note that the important difference in conductivity
482 between basalts and rhyolites (Figure 7) is predominantly due to differences between their heat
483 capacities and densities, while their thermal diffusivities are found similar (Figure 6).
484
485 **Interpretation of results**
486
487 General Temperature dependence

488 For all compositions investigated in this study, thermal diffusivities decrease with increasing
489 temperature until reaching a plateau at temperatures between 700 and 1000 K. Based on experiments
490 performed at room pressure, it was observed that the plateau occurs at about the Debye temperature
491 of the mantle minerals (Hofmeister et al. 2009, 2014). For this reason, it was proposed that thermal
492 diffusivities vary largely with temperature until the complete activation of the vibration modes
493 (phonons in minerals). The temperature range observed in our study for the occurrence of a plateau
494 is fully compatible with this interpretation.

495 For basaltic glasses, a comparable but more moderate decrease of thermal diffusivity was
496 reported up to a saturation temperature corresponding well to the glass Tg (Hofmeister et al. 2009,
497 2014, Romine et al. 2012). In our experiments, the decrease is of ~30% to 60% over the investigated
498 temperature range, depending on the experiment. Such amplitude is compatible with the ~40%
499 decrease observed during the heating of pyroxene glasses (Hofmeister et al. 2009).

500 For rhyolite samples, the thermal conductivity increases slightly with increasing the temperature
501 (Figure 7). This is due to the heat capacity that increases more with temperature than the density
502 increases and diffusivity decreases (Eq. 17). The increase is, however, smaller than reported in
503 Romine et al. (2012), due to the use of a different Cp (Neuville et al. 1993) (see Supplementary Text
504 S4) and a stronger temperature dependence of thermal diffusivities observed in our experiments
505 because of different crystallizations states.

507 <u>Effect of radiative conduction</u>
508 Romine et al. (2012) reported an increase in thermal diffusivities of the melts at very high
509 temperatures at ambient pressure. They attributed this feature to an increased role of the radiative
510 component. Such a component can dominate the thermal diffusivity for a sample transparent to the
511 infrared and visible photons at high temperatures. For thin samples, this effect can become
512 problematic if the mean free path of photons is longer than the sample length (ballistic photons, see
513 Hofmeister and Branlund, 2015). No significant increase in thermal diffusivity and conductivity is
514 observed in our high-pressure experiments, except maybe for the rhyolitic samples (Figures 6 and 7).
515 The difference with the previous work is most probably related to the opacity of our basalts and
516 peridotites samples, hence limiting the radiative transfers.

518 <u>Effect of glass/melt composition</u>
519 Overall, our conductivity values are compatible with the values available in the literature (see
520 Figure 8). Differences in absolute values are nonetheless present. Rhyolite melts (0.31-0.41 W/m/K)
521 are found slightly more conductive than basaltic ones (0.18-0.34 W/m/K). Within the same family of
522 glass, thermal conductivity varies by 0.10 to 0.15 W/m/K for rhyolitic and basaltic melts, respectively.
523 This is slightly larger (of at least 10%) than the experimental uncertainty, an effect possibly due to
524 larger uncertainties on the dimensions of the molten sample. No clear trend can be retrieved from the
525 comparison between our different basaltic or rhyolitic compositions. Among the major elements, iron
526 could be of major importance, due to its critical impact on glass/melt density. Indeed, the thermal
527 diffusivity of glasses was reported to decrease with increasing density (Hofmeister 2014). The
528 comparison between our rhyolites and basalts is coherent with such a trend. However, our haplobasalt
529 (M836) presents diffusivity values comparable with natural basalts (M662, M807, M844), as well as
530 Fe-bearing (M843 and M848) and Fe-free (M808 and M850) rhyolites (Figure 6), despite a variation
531 of the Fe-content from 0 to 10 wt.% in these different samples. Other elements could also impact the
532 melt thermal diffusivity, in particular Si and Al, which favor polymerization of the liquid (and alkali
533 elements for the opposite effect) (Ni et al. 2015). Still, within the experimental uncertainty, we
534 observe no clear trend related to these elements, despite a variation of the SiO_2 content by more than
535 20%. Additionally, water, with a total content smaller than 1.10 wt.%, should have a negligible effect
536 on thermal conductivity (Romine et al. 2012, Ni et al. 2015). It could, however, impact the melt
537 density at a low degree of partial melting (Hofmeister 2014). As the water contents estimated in the

538 recovered samples are similar to the ones obtained in starting materials (see Supplementary Text S2
539 and S3), water should not induce any strong diffusivity variation in our data-set. We, therefore,
540 conclude that chemical effects are secondary compared to the structural ones.
541
542 <u>Mixing models for thermal conductivities of partially molten peridotite</u>
543   Our results show that peridotites, and to a lower extent the glasses, present higher thermal
544 diffusivities compared to the melts. This result is not surprising: thermal conductivity is strongly
545 dependent on the local structure and its vibrational properties. The disorder in the atomic structure
546 increases from solid, glasses to molten states (Hofmeister et al. 2014). The composition of the melt
547 appears to be of secondary importance. The final set of thermal diffusivities and conductivities values
548 selected for the applications are given in Tables 3, S5 and Figures 9 and S14.
549   To propose a predictive law for thermal conductivity of partially molten rocks several mixing
550 equations are now tested. Such equation generally describes the effect of a small amount of
551 conductive phase into an insulating matrix. For thermal conduction, the problem is reversed because
552 the melt is less conductive than the solid. In this section, we explore the different predictive models
553 of thermal conductivity of binary mixtures:
554 1) Linear mixing model consider parallel thermal resistor:

$$\kappa_{bulk} = \kappa_s * (1 - F) + F\kappa_m (18)$$

556 Where s corresponds to the solid, m the melt and F the volume fraction of the melt.
557 2) tube / Ashbie model consider 1/3 of tubes of melt aligned in the heat flow direction (Grant and
558 West, 1965, Schmeling 1986):

$$\kappa_{bulk} = \frac{1}{3} * \kappa_s * (1 - F) + F\kappa_m \ (19)$$

560 3) cube model (Waff, 1974) representing cubes of solids into a melt matrix

$$\kappa_{bulk} = [1 - F^{2/3}] * \kappa_s \ (20)$$

562 4) Archie's law, an empirical relation developed for electrical conductivity (Watanabe and Kurita,
563 1983)

$$\kappa_{bulk} = C * (1 - F)^n * \kappa_s (21)$$

565 Where C and n are constants.
566 5) Thermal resistors in series:

$$\kappa_{bulk} = \kappa_s * \frac{\kappa_m/\kappa_s}{\kappa_m/\kappa_s + F(1 - \kappa_m/\kappa_s)} (22)$$

568 6) Hashin Shtrikman lower bound (HS⁻), representing insulating melt spheres into a conductive solid
569 matrix:

$$\kappa_{bulk} = \kappa_s * \frac{F}{1/(\kappa_m/\kappa_s) + \frac{1 - F}{3\kappa_s}} (23)$$

571 7) Maxwell-Eucken relation:

$$\kappa_{bulk} = \kappa_s * \frac{\kappa_m + 2\kappa_s + 2F(\kappa_m - \kappa_s)}{\kappa_m + 2\kappa_s - F(\kappa_m - \kappa_s)} (24)$$

573
574 8) Landauer relation, based on resistors in series:

$$\kappa_{bulk} = \frac{1}{4} * \left[\kappa_m(3F - 1) + \kappa_s(2 - 3F) + \left\{ (\kappa_m(3F - 1) + \kappa_s(2 - 3F))^2 + 8\kappa_s\kappa_m \right\}^{\frac{1}{2}} \right] (25)$$

576
577 9) Russel-Rayleigh relation:

$$\kappa_{bulk} = \frac{\kappa_s[\kappa_s + F^{2/3}(\kappa_m - \kappa_s)]}{\kappa_s + (\kappa_m - \kappa_s)(\kappa_m^{\frac{2}{3}} - F)} (26)$$

579

580 These equations provide a different evolution of the thermal conductivity with the fraction of melt
581 (F). In Figure S14, we present the results when either fixing κ_{solid} and κ_{melt} to the average value of our
582 measurements, or adjusting their values to minimize the misfit between the mixing models and our
583 results at varying F values (Table S5). Among the variety of fits obtained, it appears that the effect of
584 partial melting is underestimated in most of the cases. Only the thermal resistors in series is capable
585 to reproduce adequately the strong curvature observed experimentally at low F values, as well as the
586 end-member values of solid and melt conductivities. For this reason, we use series model (eq. 22) for
587 further discussions.
588   We note a lack of data points at high melt fractions, preventing to decipher more precisely the
589 mixing trend. At very high temperatures, the experimental measurements become difficult on natural
590 peridotite melting, in particular due to melt escape and chemical reactions with the experimental cell.
591 Complementary data could be acquired working with analog system such as basalt/olivine mixture
592 and could represent a further research direction.
593
594 <u>Thermal conductivity of partially molten peridotite: influence of texture</u>
595   The 3D solid/melt arrangement is known to influence significantly the geophysical properties
596 of partially molten systems (von Bargen and Waff, 1986; Laporte et al., 1997; Laporte and Provost,
597 2000, Minarik and Watson, 1995; Yoshino et al., 2005 Maumus et al. 2005; Ten Grotenhuis et al.
598 2005, Freitas et al. 2019). Their distribution is classically described using dihedral angle value, which
599 translates the ability of a liquid to wet the grain boundaries as a consequence of interfacial energies.
600 The dihedral angle decreases when increasing pressure, temperature, water content and decreasing
601 silica/alumina content of the melt (Yoshino et al. 2007, Mibe et al. 1998, 1999, Laporte et al., 1997,
602 Watson et al 1991). Several studies with similar basaltic or peridotite melts (dry) have shown that
603 basalt-like melts at mantle conditions have dihedral angles significantly lower than the
604 interconnection threshold of 60°, with values between 30-40° at 2 GPa (Laporte et al., 1997, Yoshino
605 et al. 2005, 2007). Our partially molten samples display a coherent texture and dihedral angles with
606 these observations. Dihedral angles of 23.3° and 19.0° were measured from our samples containing
607 6.4% and 23.3% of melt, respectively (Figure S15), in good agreement with previous data given that
608 these mafic melts are moderately hydrous (Table S3). For each melt fraction, a thin layer of melt
609 surround most of the grains, in particular olivines, which in 3D will result into the insulation of the
610 solid gains from their surroundings (Figure S9). This is very well visible on our low melt fraction
611 sample (F=6.4%) where the layers of melt are few microns thick (M804). Even if melt is more
612 abundant near clinopyroxenes and spinel sites in M847 (F=23.3%), the melt pockets are
613 interconnected with similar thin melt layers (<10 µm) (Figure S9). As a result, thermal conductivity
614 is expected to drop brutally in the first degrees of melting. Still, some grain boundaries should remain
615 un-wetted until the melt fraction rise significantly. For this reason, thermal conductivity should only
616 stabilize at melt fraction corresponding to solid grains completely isolated from each other. This trend
617 is visible in our data and parallel model (Figures 9 and S14) with a strong decrease in the first 10%
618 of melting highlighted by M804, the change of slope seems to occur around 15% and values decease
619 more slowly in the 15-50% range as seen in M847, to stabilize and display near-melt values above
620 50%. The complete isolation of solids should occur at "packing" threshold, which is a function of the
621 solid shapes and size distribution and is expected to occur between 40 to 60% of melting. Thus, the
622 first degrees of melting are very crucial in the case of a wetting liquid and affecting importantly the
623 thermal properties.
624
625 <u>Thermal conductivity of peridotite: effect of the grain size</u>
626   The modelling of thermal conductivity of peridotites and low F molten peridotites should also
627 take in account the effect of grain boundaries thermal resistances as grain size may vary in the
628 different geological contexts (from 100 µm to >1 cm), as seen in natural meteoritic examples, (Barrat
629 et al. 1999, Busek, 1977, Keil, 2010, Floran et al. 1978). Indeed, grain boundary scattering could be

important when the mean free paths of phonons approach the grain size. This effect, which only concerns solids and low fractions of melt, can be quantified with the following equation (Smith et al. 2003, Smith et al. 2013):

$$\frac{1}{\kappa_{poly}} = \frac{1}{\kappa_{single}} + nR_{boundary} \quad (27)$$

Where κ_{poly} is the thermal conductivity of the polycrystalline sample, κ_{single} the thermal conductivity of a reference single crystal (average from olivine data of Hofmeister et al. 2016, Table 3), n represents the surface of grain boundaries along the heat flow direction per unit length, and $R_{boundary}$ the thermal resistance of grain boundary plane. The n value should be almost constant with temperature (Smith et al. 2013) and is estimated between $4e^{-4}$ and $7e^{-3}$ m for our two peridotite samples via analyses of SEM images (grain size ranging from 25 to 140 µm, see Table S4 for textural parameters). We calculate $R_{boundary}$ values between $1.9e^{-6}$ and $5.9e^{-6}$ W/m²/K for M804 and $9.3e^{-6}$ and $3.2e^{-5}$ W/m²/K for M847. These values are compatible or slightly higher than hydrous polycrystalline olivine samples (Zhang et al. 2019).

As a result, the thermal conductivities quantified in our experiments are underestimations of natural ones as the grain size is <100 µm, in experiments compared to grain sizes of 100 µm up to >1 cm typical of mantle peridotites and reduced meteorites (which could be relic of bodies interiors, from cumulates (Floran et al. 1978), enstatite chondrite/achondrite (Keil, 2010), diogenite (Barrat et al. 1999) to pallasite (Busek, 1977)). Melts and high F partially molten systems are not affected by such effect, thus the observed decrease of thermal conductivity at the melting temperature is probably smaller in our experiments.

Implications for geodynamos on Mercury-like proto-planets

Suitable conditions for a dynamo

For a thermally driven dynamo to operate in a terrestrial planet, four conditions were found to be necessary (e.g., Monteux et al., 2011): the core heat flow must be at least adiabatic (1), the thermal convection within the core has to supply enough power to compensate the losses due to ohmic dissipation (2), the Reynolds magnetic number must be supercritical (complex turbulent convection) (3) and the mantle heat flow has to overcome the core heat flow needed to induce a dynamo (4). These conditions can be expressed in terms of heat flow balance (See Figure 10 for a schematic representation) and are detailed here:

(1) The metallic core has to convect, meaning that the heat flow out of the core needs to overcome the adiabatic heat flow (Stevenson et al., 1983).

For this, the core thermal conductivity (κ_{core}) is a dominant parameter. A large κ_{core} value increases the heat flux along the core adiabat and reduces the lifetime of a thermally driven dynamo (Breuer et al., 2015). Several laboratory measurements suggested that the thermal conductivity of polycrystalline iron at Mercury's core conditions is 113–125 W/m/K (see Deng et al., 2013 and references therein). However, such values for Mercury are recently challenged with several recent studies proposing a much lower conductivity. In a first one, the conductivity of pure Fe and Fe-Si alloys is reported at 30-40 W/m/K and 35-40 W/m/K, respectively (Sibert et al. 2019). Then, it is proposed that the thermal conductivity of Fe-S at the P-T conditions of Mercury's core is as low as ~4 W/m/K, thus 1-2 orders of magnitude lower than that of pure iron (Pommier et al. 2019, Manthilake et al. 2019).

This first condition can be expressed as:

$$Q_{CMB} > Q_{Ad} = \frac{\kappa_c \alpha_c g_c T_{CMB}}{C_{p,c}} 4\pi R_c^2 \quad (28)$$

To estimate this flux, we assume that T$_{CMB}$ is the melting temperature of pure iron at P$_{CMB}$. This assumption gives a conservative value of the core heat flow in comparison with considering T$_{ICB}$ since the core liquidus is steeper that the core adiabat. We estimate the relation between the melting temperature of pure iron and the pressure using the following expression obtained by fitting the experimental results from Anzellini et al. 2013 with a Simon and Glatzel equation:

$$T_{m,Fe} = 1800\left(\frac{P_{CMB}}{27.9} + 1\right)^{1/2.08} \quad (29)$$

Such a melting temperature typically lies between the solidus and liquidus of a chondritic mantle for the same pressure conditions (Monteux et al. 2020 and references therein). We also assume that k_c, α_c and $C_{p,c}$ are constant (see values in Table 4) and P_{CMB} is calculated as follows (Monteux and Arkani-Hamed, 2014):

$$P_{CMB} = P(r = R_c) = \frac{2}{3}\pi G \rho_c^2 (R_c^2 - r^2) + \frac{2}{3}\pi G \rho_{Si}^2 (R^2 - R_c^2) + \frac{4}{3}\pi G \rho_{Si} R_c^3 (\rho_c - \rho_{Si})\left(\frac{1}{R_c} - \frac{1}{R}\right) \quad (30)$$

(2) The energy supplied by thermal convection to the geodynamo has to compensate for the loss due to ohmic decay (Buffett, 2002).

This imposes a condition on the core heat flow at the CMB. In fact, core heat flow will need to overcome a critical value. Assuming that dynamo is generated only by thermal convection in the core, we can write:

$$Q_{CMB} > Q_{Ad} + \frac{4 v_c \bar{B}^2 C_{p,c}}{0.8 \mu_c \alpha_c G \rho_c R_c} \quad (31)$$

This heat flux is estimated by considering that the characteristic magnetic length scale equals the radius of the core. The parameter $\bar{B}$ is the average strength of the magnetic field inside the core and was estimated using a scaling from Christensen and Aubert (2006):

$$\bar{B} = 0.9 \mu_c^{\frac{1}{2}} \rho_c^{\frac{1}{6}} \left(\frac{g_c Q_B (R_c - r_i)}{4\pi R_c r_i}\right)^{\frac{1}{3}} \quad (32)$$

With $Q_B = \alpha_c Q_{CMB}/C_{p,c}$ the buoyancy flux and r_i the radius of the inner core. In the scaling from Christensen and Aubert (2006), the inner core size cannot be set to 0. On Mercury the size of the inner core is currently not well constrained even if recent constraints via geodetic analysis (Genova et al. 2018) suggest its presence and a possible important size (r_i/R_c between 0.3 and 0.7). As we focus here on the effect of thermal cooling on dynamo generation (i.e. we do not consider the effect of compositional convection related to inner core growth), we consider a small inner core with $r_i/R_c = 0.01$. The scaling law used to calculate the average strength of the magnetic field inside the core (Eq. 32) is valid for the Earth but overestimates $\bar{B}$ in the case of thin shell dynamos such as the one operating within Mercury (Christensen and Aubert (2006)). Mariner 10 spacecraft measurements showed that Mercury's magnetic field was 100 times weaker than the Earth's one. To account for this discrepancy, we consider that the average strength of the magnetic field is $1\%\bar{B}$ obtained from Eq. 32 when solving Eq. 31. We also consider that v_c, μ_c and ρ_c are constants (see values in Tab. 4). We note that most of the power needed to overcome the criterion related to Eq. 31 can be supplied by thermal core convection (i.e. criterion related to Eq. 28) especially for large metallic cores.

(3) The magnetic Reynolds number (Re$_m$) must be supercritical in order to have convective motions, inducing a complex structure needed to carry the magnetic field lines (U. R. Christensen and Aubert, 2006).

Reynolds magnetic number is calculated using Christensen and Aubert, 2006 formulation's and assuming that the characteristic magnetic length scale is the radius of the core:

$$Re_m = \left(\frac{Q_{CMB} G \alpha_c}{3 C_{p,c}}\right)^{1/3} \frac{R_c}{v_c} > 10 - 100 \quad (33)$$

The value of the critical magnetic Reynolds number ($Re_{m,c}$) is usually constrained for models implying a large inner core. For Mercury-like planets, this value is less documented. Here we make the conservative assumption that this value ranges between 10 and 100.

(4) The mantle heat flow has to overcome the core heat flow needed to generate a dynamo.

The mantle's Rayleigh number (Ra) conditions the efficiency of heat evacuation from the mantle:

$$Ra = \frac{\alpha_{Si}\rho_{Si}g\Delta T \delta_{Si}^{3}}{\eta_{Si}\kappa_{Si}} \quad (34)$$

With α_{Si} the mantle thermal expansion coefficient, ρ_{Si} the mantle density, ΔT the temperature difference between the core and the surface of the planet, δ_{Si} the mantle thickness, η_{Si} the mantle viscosity, κ_{Si} the mantle heat diffusivity ($\kappa_{Si} = k_{Si}/(\rho_{Si}C_{p,Si})$), and $C_{p,Si}$ the mantle heat capacity. If Ra is lower than a critical value ($Ra_C \approx 1000$), the heat is evacuated from the mantle by conduction and the mantle heat flow Q_{Si} is:

$$Q_{Si} = \frac{k_{Si}\Delta T}{\delta_{Si}} 4\pi R^2 \quad (35)$$

Alternatively, if the $Ra > Ra_C$, the heat is evacuated from the mantle by convection and Q_{Si} scales with $Ra^{1/3}$ *(Solomatov, 2007)*:

$$Q_{Si} = 0.089 \frac{k_{Si}\Delta T}{\delta_{Si}} 4\pi R^2 Ra^{1/3} \quad (36)$$

In any case, for a thermally-driven dynamo to operate, Q_{Si} has to be larger than the core heat flow Q_{Core}. For these calculations, we consider here that the surface gravity is dominated by the gravity at the CMB ($g = g_c$). On a planet with a core over planet radius ratio (R_c/R) of ~0.5, the mantle is thick enough so that $Ra > Ra_c$ and the heat is efficiently evacuated by convection. On such bodies, the dynamo is generated easily and should appear early in the planet history. If the heat evacuation is very efficient, the planet might cool down rapidly, which can potentially lead to a short-lived dynamo. On a Mercury-like body with a large R_c/R ratio, the mantle is thin compared to the core and its Rayleigh number, critical criterion for thermal convection, hardly overcomes Ra_c. Hence, conduction should be the main heat evacuation process within the mantle of Mercury-like planets, which can limit the occurrence of an early thermally-driven dynamo.

Simulation results

We now compare the core heat flow needed to generate a dynamo within a Mercury-like body (with e.g. $R_c/R_{planets}$) (Figures 11 and 12). To do this, we use a maximum possible range of solid conductivities between $\kappa_{Si} = 4.32$ and 1.70 W/m/K. We consider a maximum planet radius R=2440 km with a thin mantle shell to stay in temperature and pressure conditions equivalent to the experimental conditions detailed above (P≤2GPa and T≤1700K). We also report the critical size of the protoplanet (R = 215 km) above which Re_m is larger than 100 (Eq. 33). The Figure 11 shows that a solid conductive mantle is able to evacuate enough heat to induce a thermally driven dynamo if the planet radius is larger than ~215 km, regardless of the value of thermal conductivity in the outer core, at least up to more than 40 W/m/K. In contrast, the change of core conductivities from e.g 40 W/m/K (Sibert et al., 2019) to 4 W/m/K (Manthilake et al. 2019) has a major effect on the maximum size of a planet that can operate a thermally driven dynamo. For a core conductivity $\kappa_{core} = 40$ W/m/K, the maximum planet radius evolves from 1220 to 1880 km, for $\kappa_{Si} = 1.70$ and 4.32 W/m/K, respectively. When $\kappa_{core} = 4$ W/m/K, the maximum planet radius is more than 2500 km.

We now perform the same type of calculation for a mushy mantle using the silicate-melt conductivity refined in this study (Tables 3 and 4). We consider here neither a complete magma ocean that would evacuate the core heat very efficiently by turbulent convection (Monteux et al., 2016) nor a mushy mantle with a large melt fraction (larger than 40-60%) which would imply a strong decrease of the bulk viscosity of the mantle (Picard et al., 2013). We consider here a purely conductive mantle where the melt fraction is smaller than 20%. Hence, if this melt fraction is concentrated at the core

mantle boundary, the molten layer is thin enough to avoid its convection, while if the liquid is equally distributed within the mantle, we can reasonably assume that the bulk viscosity is weakly affected by the liquid phase and close to the viscosity of subsolidus silicate material. Still, the presence of melt may affect mantle properties. An important parameter is the fate of melts, which is primarily controlled by the solid-melt density contrast. The molten material can either be evacuated at the surface during early volcanism or cumulate at the lowermost mantle. For peridotites, negative melt buoyancy is unlikely to happen at pressures lower than 7 GPa (Sakamaki et al. 2006, Matsukage et al. 2005, Freitas et al. 2017). However, the buoyancy of melts generated from the partial melting of a body with composition largely different from peridotite remains uncertain. Molten reservoirs may be trapped at shallow depths at the end of mushy mantle cooling (Monteux et al., 2020) or during the last stages of fractional crystallization within small bodies (e.g. Frossard et al., 2019). On a Moon-like body, a melt layer may be trapped below an anorthositic crust while on a Mercury-like body, anorthite is denser than the melt and then may not float allowing the melt to form a late shallow magma ocean. We consider here that the melt has neutral buoyancy and is equally distributed within the planetary mantle, with the consequence that the mantle viscosity is primarily controlled by the solid fraction of the mantle.

Due to the lower thermal conductivity of the melt compared to the solid mantle, the mushy mantle should limit the heat flow that can be extracted from the core. In our calculation, we consider for simplicity that the entire mantle has the same conductivity as the melt. As a result, the range of planetary radii for which a dynamo is plausible is much narrower than for a fully solid mantle (Figure 12). For a core conductivity of 40 W/m/K, a thermally driven dynamo can only operate for planetary sizes ranging between 215 and 350-570 km, depending on the value of κ_{Si} and for $\kappa_{core} = 40$ W/m/K. The maximum planetary radius becomes 1000-1500 km for a core conductivity of 4 W/m/K. Therefore, the melting of a Mercury-like planetary mantle could limit the establishment of a magnetic field on the planet. This effect could last over different timescales, depending on the size of the planet and of the core, the initial core temperature, the fate of the melt material, etc.

The differences obtained for fully solid (Figure 11) and molten (Figure 12) models show that the presence of melt within a "Mercury-like" planet mantle could result into better thermal insulation of the core, which may prevent the occurrence of a thermally driven dynamo. Of course, planets presenting mantle with supercritical Rayleigh number would not be affected by this effect, because mantle convection could extract enough heat from the core at the CMB. As a consequence, the solid mantle viscosity plays a key role because (1) it controls the planet size above which mantle convection is likely, through the Ra value, and (2) it governs the efficiency of mantle heat evacuation once the critical Rayleigh number is overcome (see Eq. 36). Decreasing the mantle viscosity from 10^{22} to 10^{18} Pa.s decreases the critical planet size for mantle convection by one order of magnitude (from 1600-1900 km to 160-200 km for a solid mantle and from 850-1050 km to 80-110 km for a mushy mantle, see Figures 11 and 12). The figures also show that the lower is mantle viscosity, the easier the planet can meet the criteria for a thermally driven dynamo when the mantle of the planet is convecting. We note here that considering the influence of melt on the bulk mantle viscosity should lead to a decrease of the critical Rayleigh number and as a consequence of the critical planetary size where heat in only evacuated by thermal conduction (i.e. green triangles would move to the left). However, this effect should be negligible for the small melt fraction considered here.

The impact of mantle partial melting crucially depends on the melt quantity and its location within the mantle. Whether it is distributed in a mushy mantle or accumulated as a pond at a given mantle depth affects both, locally and globally, the mantle viscosity and the thermal diffusivity. As a consequence, the dynamic regime can evolve from conduction to convection, changing the thermal outputs at the CMB and making the heat flux enough, or insufficient, to power a thermally-driven dynamo. In this framework, transient phenomena such as mantle overturns (Elkis-Tanton et al. 2003, Ballmer et al. 2017) implying major melt migration will result in a brutal change in the planet magnetic signature. Similarly, the chemical stratification resulting in the production of a crust

(anorthositic, basaltic etc.) may help insulating the planet interior in its early history suggesting weaker but longer sustained dynamos.

Conclusions

In this study, we constrain the thermal diffusivities of silicate melts with a wide range of composition at high pressure and temperature conditions using the multi-anvil apparatus and the Angström method. We observed that melting induces a significant decrease in both thermal diffusivities and conductivities. We measure melt thermal diffusivities ranging from 0.18 ($\pm$0.02) W/m/k to 0.41 ($\pm$0.04) W/m/K. The composition of the melt does not have a significant impact on diffusivities. We then use our results to address the thermal properties of the molten silicate reservoirs, and the likeliness of a thermally driven dynamo within a Mercury-like planets presenting a large metallic core and a relatively thin silicate mantle (large Rc/Rplanet). The mantle of such bodies is not expected to be convecting easily ($Ra<Ra_c$) leading to an inefficient heat evacuation and difficulty generating a dynamo compared to planets with a thicker mantle (where easily $Ra>Ra_c$). Our results illustrate that the presence of a mushy mantle above the CMB in such a Mercury-like planet can significantly reduce the ability of the mantle to evacuate the heat from the core and limit the likeliness of a thermally-driven dynamo. As a consequence, the fate and the lifetime of such a mushy reservoir can have a profound impact on the thermal history of Mercury-like planets. Future observations of Mercury-like planets accreted in orbits close to their star and the eventual detection of their intrinsic magnetic field would in return constrain the state of the mantle surrounding their metallic core.

18

References

1. Acuna, M. H., Connerney, J. E. P., Lin, R. P., Mitchell, D., Carlson, C. W., McFadden, J., et al. (1999). Global distribution of crustal magnetization discovered by the Mars Global Surveyor MAG/ER experiment. Science, 284(5415), 790–793.

2. Anderson, B. J., Johnson, C. L., Korth, H., Purucker, M. E., Winslow, R. M., Slavin, J. A., et al. (2011). The global magnetic field of Mercury from MESSENGER orbital observations. Science, 333(6051), 1859–1862. https://doi.org/10.1126/science.1211001

3. Andrault, D., Bolfan-Casanova, N., Nigro, G.L., Bouhifd, M.A., Garbarino, G., Mezouar, M., (2011). Solidus and liquidus profiles of chondritic mantle: implication for melting of the Earth across its history. Earth Planet. Sci. Lett.304, 251–259. http://dx.doi.org/10.1016/j.epsl.2011.02.006.

4. Anzellini, S., Dewaele, A., Mezouar, M., Loubeyre, P., Morard, G., (2013). Melting of iron at Earth's inner core boundary based on fast X-ray diffraction. Science340, 464–466.

5. Asphaug, E., & Reufer, A. (2014). Mercury and other iron-rich planetary bodies as relics of inefficient accretion. Nature Geoscience, 7(8), 564–568. https://doi.org/10.1038/ngeo2189

6. Bajgain, S., Ghosh, D. B., & Karki, B. B. (2015). Structure and density of basaltic melts at mantle conditions from first-principles simulations. Nature Communications, 6, 1–7. https://doi.org/10.1038/ncomms9578

7. Ballmer, M. D., D. L. Lourenco, K. Hirose, R. Caracas, and R. Nomura (2017), Reconciling magma-ocean crystallization models with the present-day structure of the Earth's mantle, Geochem., Geophys., Geosyst., 18(7), 2785-2806, doi:10.1002/2017gc006917.

8. Bambier, A., Berger, E., Mergoil, J., Valadas, B., Veyret, Y., Weisbord, A., (1985). Carte géologique de la France à 1/50 000 (n 840), Burzet: Des sources de l'Ardèche aux sources de la Loire. Carte et notice explicative.

9. Barrat, J.A, Gillet, PH, Lesourd, M., Blicher-Toft, J., & G.R Poupeau. (1999). The Tatahouine diogenite: Mineralogical and chemical effects of sixty-three years of terrestrial residence. Meteoritics & Planetary science, 34, 91-97.

10. Beck, A. E., Darbha, D. M., & Schloessin, H. H. (1978). Lattice conductivities of single-crystal and polycrystalline materials at mantle pressures and temperatures. Physics of the Earth and Planetary Interiors, 17(1), 35–53. https://doi.org/10.1016/0031-9201(78)90008-0

11. Benz, W., Slattery, W. L., & Cameron, A. G. W. (1988). Collisional stripping of Mercury's mantle. Icarus, 74(3), 516–528. https://doi.org/10.1016/0019-1035(88)90118-2

12. Berger, E., (1973). Le volcanisme récent de l'Ardèche. Thèse, Orsay, 402 p.

13. Berger, E., Forette, M. C., (1975). Réactions de basaltes alcalins des Causses, du Vivarais et du Velay (France) avec les xénocristaux et les minéraux des enclaves homoéogènes. Bulletin de Minéralogie, 98(6), 366-373.

14. Berger, E., (1981). Enclaves ultramafiques, mégacristaux et leurs basaltes-hôtes en contexte océanique (Pacifique Sud) et continental (Massif Central Français). Thèse d'État, Université de Paris-Sud, Orsay,470 p.

15. Bigazzi, G., Yegingil, Z., Ercan, T., Oddone, M., Özdogan, M., (1993). Fission track dating obsidians in Central and Northern Anatolia. Bulletin of Volcanology, 55(8), 588-595.

887   16.   Bolfan-Casanova, N., Montagnac, G., Reynard, B., (2014). Measurement of water contents in olivine
888   using Raman spectroscopy. Am. Mineral. 99:149–156. doi: 10.2138/am.2014.4444.
889   17.   Bougault, H., & Treuil, M. (1980). Mid-atlantic ridge: Zero-age geochemical variations between azores
890   and 22°N. Nature, 286(5770), 209–212. https://doi.org/10.1038/286209a0
891   18.   Boujibar, A., Andrault, D., Ali, M., Bolfan-casanova, N., Devidal, J., & Trcera, N. (2014). Metal –
892   silicate partitioning of sulphur , new experimental and thermodynamic constraints on planetary
893   accretion. Earth and Planetary Science Letters, 391, 42–54. https://doi.org/10.1016/j.epsl.2014.01.021
894   19.   Boujibar, A., Andrault, D., Bolfan-Casanova, N., Bouhifd, M. A., & Monteux, J. (2015).
895   Cosmochemical fractionation by collisional erosion during the Earth's accretion. Nature
896   Communications, 6, 1–7. https://doi.org/10.1038/ncomms9295
897   20.   Breuer, D., Hauck, S. A., Buske, M., Pauer, M., Spohn, T., (2007). Interior Evolution of Mercury. Space
898   Sci. Rev. 132, 229–260.
899   21.   Breuer, D., Rueckriemen, T., & Spohn, T. (2015). Iron snow, crystal floats, and inner-core growth:
900   modes of core solidification and implications for dynamos in terrestrial planets and moons. Progress in
901   Earth and Planetary Science, 2(1), 39. https://doi.org/10.1186/s40645-015-0069-y
902   22.   Buffett, B.A., 2002. Estimates of heat flow in the deep mantle based on the power requirements for the
903   geodynamo. Geophys. Res. Lett. 29 (12), 1–4.
904   23.   Busek, P. R., (1997). Pallasite meteorites-mineralogy, petrology and geochemistry. Geochimica et
905   Cosmochimica Acta, 41, 711-740.
906   24.   Cao, H., Aurnou, J. M., Wicht, J., Dietrich, W., Soderlund, K. M., & Russell, C. T. (2014). A dynamo
907   explanation for Mercury's anomalous magnetic field. Geophysical Research Letters, 41, 4127–4134.
908   https://doi.org/10.1002/2014GL060196.
909   25.   Charlier, B., and Namur, O., (2019). The Origin and Differentiation of Planet Mercury, Elements, 15
910   (1): 9–14. https://doi.org/10.2138/gselements.15.1.9.
911   26.   Chen, B., Li, J., & Hauck, S. A. (2008). Non-ideal liquidus curve in the Fe-S system and Mercury's
912   snowing core. Geophysical Research Letters, 35, L07201. https://doi.org/10.1029/2008GL033311.
913   27.   Christensen, U. R., & Aubert, J. (2006). Scaling properties of convection-driven dynamos in rotating
914   spherical shells and application to planetary magnetic fields. Geophysical Journal International, 166(1),
915   97–114. https://doi.org/10.1111/j.1365-246X.2006.03009.x
916   28.   Christensen, U. R., & Wicht, J. (2008). Models of magnetic field generation in partly stable planetary
917   cores: Applications   to   Mercury   and   Saturn.   Icarus,   196(1),   16–34.
918   https://doi.org/10.1016/j.icarus.2008.02.013.
919   29.   Christensen, U. R. (2006). A deep dynamo generating Mercury's magnetic field. Nature, 444(7122),
920   1056–1058. https://doi.org/10.1038/nature05342.
921   30.   Deng, L., Seagle, C., Fei, Y., & Shahar, A. (2013). High pressure and temperature electrical resistivity
922   of iron and implications for planetary cores. Geophysical Research Letters, 40, 33–37.
923   https://doi.org/10.1029/2012GL054347.
924   31.   Druitt, T. H. (1995). Settling behaviour of concentrated dispersions and some volcanological
925   applications.   Journal   of   Volcanology   and   Geothermal   Research,   65(1–2),   27–39.
926   https://doi.org/10.1016/0377-0273(94)00090-4
927   32.   Dumberry, M., & Rivoldini, A. (2015). Mercury's inner core size and core-crystallization regime. Icarus,
928   248, 254–268. https://doi.org/https://doi.org/10.1016/j.icarus.2014.10.038.
929   33.   Ebel, D. S., & Grossman, L. (2000). Condensation in dust-enriched systems, 64(2), 339–366.
930   34.   Elkins-Tanton, L. T., E. M. Parmentier, and P. C. Hess (2003), Magma ocean fractional crystallization
931   and cumulate overturn in terrestrial planets: Implications for Mars, Meteoritics & Planetary Science,
932   38(12), 1753-1771, doi:10.1111/j.1945-5100.2003.tb00013.x.

933 35. Fegley, B., & Cameron, A. G. W. (1987). A vaporization model for iron/silicate fractionation in the
934   Mercury protoplanet. Earth and Planetary Science Letters, 82(3–4), 207–222.
935   https://doi.org/10.1016/0012-821X(87)90196-8

936 36. Floran, R.J., Prinz M., Hlava, P.F., Keil, K., Nehru, C.E. & Hinthorne. J. R. (1978). The Chassigny
937   meteorite: a cumulate dunite with hydrous amphibole-bearing melt inclusions. Geochemica et
938   Comsochimica acta, 42 (8), 1213-1219. https://doi.org/10.1016/0016-7037(78)90115-1

939 37. Freitas, D., Manthilake, G., Schiavi, F., Chantel, J., Bolfan-Casanova, N., Bouhifd, M.A., Andrault, D.,
940   (2017).Experimental evidence supporting a global melt layer at the base of the Earth's upper mantle.
941   Nat.Commun. 8:2186. https ://doi.org/10.1038/s4146 7-017-02275 -9.

942 38. Freitas, D., Manthilake, G., Chantel, J., Bouhfid, M.., Andrault, D., (2019). Simultaneous measurements
943   of electrical conductivity and seismic velocity of partially molten geological materials: Implications for
944   melt fraction in the upper mantle. Phys. Chem. Miner. 0, 0. doi:10.1007/s00269-019-01021-5.

945 39. Freitas, D., Manthilake, G., (2019b). Electrical conductivity of hydrous silicate melts : Implications for
946   the bottom-up hydration of Earth ' s upper mantle EPSL 523, 1–9. doi:10.1016/j.epsl.2019.115712.

947 40. Frossard P., Boyet M., Bouvier A., Hammouda T., Monteux J. (2019). Evidence for anorthositic crust
948   formed on an inner solar system planetesimal. Geochemical Perspectives Letters vol.11, p.28-32,
949   DOI:10.7185/geochemlet.1921 .

950 41. Fujisawa, H., Fujii, N., Mizutani, H., Kanmori, H., Akimoto, S., (1968) Thermal Diffusivity of
951   Mg2SiO4, Fe2SiO4, and NaCl at High Pressures and Temperatures. J. Geophys. Res. 73:4727.

952 42. Garrick-Bethell, I., Weiss, B. P., Shuster, D. L., & Buz, J. (2009). Early lunar magnetism. Science,
953   323(5912), 356–359. https://doi.org/10.1126/science.1166804

954 43. Genova, A., Goossens, S., Mazarico, E., Lemoine, F. G., Neumann, G. A., Kuang, W., et al. (2018).
955   Geodetic evidence that Mercury has a solid inner core, 1–13. https://doi.org/10.1029/2018GL081135

956 44. Gillet, P., Richet, P., Guyot, F., Fiquet, G., (1991). High-temperature thermodynamic properties of
957   forsterite. J. Geophys. Res. B96:11805–11816.

958 45. Giordano, D., Nichols, A. R. L., & Dingwell, D. B. (2005). Glass transition temperatures of natural
959   hydrous melts: A relationship with shear viscosity and implications for the welding process. Journal of
960   Volcanology and Geothermal Research, 142(1-2 SPEC. ISS.), 105–118.
961   https://doi.org/10.1016/j.jvolgeores.2004.10.015

962 46. Glassmeier, K. H., Auster, H. U., & Motschmann, U. (2007). A feedback dynamo generating Mercury's
963   magnetic field. Geophysical Research Letters, 34, L22201. https://doi.org/10.1029/2007GL031662.

964 47. Grant, F. S., West, G. F., (1965). Interpretation theory in applied geophysics. 583 pp., McGraw-Hill
965   Book Co., New York.

966 48. ten Grotenhuis, S.M., Drury, M.R., Spiers, C.J., Peach, C.J., 2005. Melt distribution in olivine rocks
967   based on electrical conductivity measurements. J. Geophys. Res. Solid Earth 110, 1–11.
968   https://doi.org/10.1029/2004JB003462

969 49. Guérin G., (1983). La thermoluminescence des plagioclases, méthode de datation du volcanisme.
970   Application au domaine volcanique français : chaîne des Puys, Mont-Dore et Cézallier, Bas-Vivarais,
971   thèse, université Paris-6, 258 p.

972 50. Harte, B., (1977). Rock nomenclature with particular relation to deformation and recrystallisation
973   textures in olivine-bearing xenoliths. The Journal of Geology, 85(3), 279-288.

974 51. Hartlieb, P., Toifl, M., Kuchar, F., Meisels, R., & Antretter, T. (2016). Thermo-physical properties of
975   selected hard rocks and their relation to microwave-assisted comminution. Minerals Engineering, 91,
976   34–41. https://doi.org/10.1016/j.mineng.2015.11.008

977 52. Hauck, S. A., Margot, J. L., Solomon, S. C., Phillips, R. J., Johnson, C. L., Lemoine, F. G., et al. (2013).
978   The curious case of Mercury's internal structure. Journal of Geophysical Research E: Planets, 118(6),
979   1204–1220. https://doi.org/10.1002/jgre.20091

21

980 53. Heimpel, M. H., Aurnou, J. M., Al-Shamali, F. M., & Gomez Perez, N. (2005). A numerical study of
981   dynamo action as a function of spherical shell geometry. Earth and Planetary Science Letters, 236(1–2),
982   542–557. https://doi.org/10.1016/j.epsl.2005.04.032.

983 54. Hernlund, J., Leinenweber, K., Locke, D., & Tyburczy, J. A. (2006). A numerical model for steady-state
984   temperature distributions in solid-medium high-pressure cell assemblies. American Mineralogist, 91(2–
985   3), 295–305. https://doi.org/10.2138/am.2006.1938

986 55. Hofmeister, A. M., & Branlund, J. M. (2015). Thermal Conductivity of the Earth. Treatise on
987   Geophysics: Second Edition (Vol. 2). Elsevier B.V. https://doi.org/10.1016/B978-0-444-53802-
988   4.00047-6

989 56. Hofmeister, Anne M., Whittington, A. G., & Pertermann, M. (2009). Transport properties of high albite
990   crystals, near-endmember feldspar and pyroxene glasses, and their melts to high temperature.
991   Contributions to Mineralogy and Petrology, 158(3), 381–400. https://doi.org/10.1007/s00410-009-
992   0388-3

993 57. Hofmeister, Anne M., Sehlke, A., & Whittington, A. G. (2014). Thermal diffusivity of Fe-rich pyroxene
994   glasses and their melts. Chemical Geology, 384, 1–9. https://doi.org/10.1016/j.chemgeo.2014.06.018

995 58. Hood, L. L., Harrison, K. P., Langlais, B., Lillis, R. J., Poulet, F., & Williams, D. A. (2010). Magnetic
996   anomalies near Apollinaris Patera and the Medusae Fossae Formation in Lucus Planum, Mars. Icarus,
997   208(1), 118–131. https://doi.org/10.1016/j.icarus.2010.01.009

998 59. Johnson, Catherine L., & Phillips, R. J. (2005). Evolution of the Tharsis region of Mars: Insights from
999   magnetic field observations. Earth and Planetary Science Letters, 230(3–4), 241–254.
1000   https://doi.org/10.1016/j.epsl.2004.10.038

1001 60. Johnson, C. L., & McFadden, P. (2015). The Time-Averaged Field and Paleosecular Variation. Treatise
1002   on Geophysics: Second Edition, 5, 385–417. https://doi.org/10.1016/B978-0-444-53802-4.00105-6

1003 61. Johnson, C. L., Phillips, R. J., Purucker, M. E., Anderson, B. J., Byrne, P. K., Denevi, B. W., et al.
1004   (2015). Low-altitude magnetic fieldmeasurements by MESSENGER reveal Mercury's ancient crustal
1005   field. Science, 348(6237), 892–895. https://doi.org/10.1126/science.aaa8720.

1006 62. Kabin, K., Heimpel, M. H., Rankin, R., Aurnou, J. M., Gómez-Pérez, N., Paral, J., et al. (2008). Global
1007   MHD modeling of Mercury's magnetosphere with applications to the MESSENGER mission and
1008   dynamo theory. Icarus, 195(1), 1–15. https://doi.org/10.1016/j.icarus.2007.11.028

1009 63. Kanamori H., Mizutani, H., Fujii, N., (1969). Method of thermal diffusivity measurement. J. Phys. Earth.
1010   17:43–53.

1011 64. Katsura, T. (1993). Thermal diffusivity of silica glass at pressures up to 9 GPa. Physics and Chemistry
1012   of Minerals, 20(3), 201–208. https://doi.org/10.1007/BF00200122

1013 65. Keil, K. (2010) Enstatite achondrite meteorites (aubrites) and the histories of their asteroidal parent
1014   bodies, Chemie der Erde, 70 (4), 295-317. doi:10.1016/j.chemer.2010.02.002

1015 66. Laporte, D., Rapaille, C., Provost, A., (1997). Wetting angles, equilibrium melt geometry, and the
1016   permeability threshold of partially molten crustal protoliths BT. In: Bouchez JL, Hutton DHW, Stephens
1017   WE (eds) Granite: from segregation of melt to emplacement fabrics. Springer Netherlands, Dordrecht,
1018   pp 31–54.

1019 67. Laporte, D., Provost, A., 2000. Equilibrium geometry of a fluid phase in a polycrystalline aggregate
1020   with anisotropic surface energies: Dry grain boundaries. J. Geophys. Res. Solid Earth 105, 25937–
1021   25953. https://doi.org/10.1029/2000jb900256

1022 68. Lawrence, K., Johnson, C., Tauxe, L., & Gee, J. (2008). Lunar paleointensity measurements:
1023   Implications for lunar magnetic evolution. Physics of the Earth and Planetary Interiors, 168(1-2), 71-87.

1024 69. Li, L., Wentzcovitch, R. M., Weidner, D. J., & Da Silva, C. R. S. (2007). Vibrational and thermodynamic
1025   properties of forsterite at mantle conditions. Journal of Geophysical Research: Solid Earth, 112(5).
1026   https://doi.org/10.1029/2006JB004546

1027   70. Lillis, R. J., Frey, H. V., Manga, M., Mitchell, D. L., Lin, R. P., Acuña, M. H., & Bougher, S. W. (2008).
1028   An improved crustal magnetic field map of Mars from electron reflectometry: Highland volcano
1029   magmatic history and the end of the martian dynamo. Icarus, 194(2), 575–596.
1030   https://doi.org/10.1016/j.icarus.2007.09.032
1031   71. Lillis, R. J., Robbins, S., Manga, M., Halekas, J. S., & Frey, H. V. (2013). Time history of the Martian
1032   dynamo from crater magnetic field analysis. Journal of Geophysical Research E: Planets, 118(7), 1488–
1033   1511. https://doi.org/10.1002/jgre.20105
1034   72. Malavergne, V., Toplis, M. J., Berthet, S., & Jones, J. (2010). Highly reducing conditions during core
1035   formation on Mercury: Implications for internal structure and the origin of a magnetic field. Icarus,
1036   206(1), 199–209. https://doi.org/10.1016/j.icarus.2009.09.001
1037   73. Malfait, W. J., Seifert, R., Petitgirard, S., Mezouar, M., & Sanchez-Valle, C. (2014). The density of
1038   andesitic melts and the compressibility of dissolved water in silicate melts at crustal and upper mantle
1039   conditions. Earth and Planetary Science Letters, 393, 31–38. https://doi.org/10.1016/j.epsl.2014.02.042
1040   74. Manthilake, G., Chantel, J., Monteux, J., Andrault, D., Bouhifd, M.A., Casanova, N.B., Boulard, E.,
1041   Guignot, N., King, A., Itie, J.P., (2019). Thermal conductivity of FeS and its implications for Mercury's
1042   long sustaining magnetic field. J. Geophys. Res. E Planets. doi:10.1029/2019JE005979
1043   75. Manthilake, M. A. G. M., De Koker, N., & Frost, D. J. (2011a). Thermal conductivity of CaGeO3
1044   perovskite   at   high   pressure.   Geophysical   Research   Letters,   38(8),   3–6.
1045   https://doi.org/10.1029/2011GL046882
1046   76. Manthilake, G. M., De Koker, N., Frost, D. J., & McCammon, C. A. (2011b). Lattice thermal
1047   conductivity of lower mantle minerals and heat flux from Earth's core. Proceedings of the National
1048   Academy   of   Sciences   of   the   United   States   of   America,   108(44),   17901–17904.
1049   https://doi.org/10.1073/pnas.1110594108
1050   77. Matsukage, K.N., Jing, Z., Karato, S., (2005). Density of hydrous silicate melt at the conditions of
1051   Earth's deep upper mantle. Nature 438, 488–91. doi:10.1038/nature04241.
1052   78. Maumus, J., Bagdassarov, N., Schmeling, H., 2005. Electrical conductivity and partial melting of
1053   mafic rocks under pressure. Geochim. Cosmochim. Acta 69, 4703–4718.
1054   https://doi.org/10.1016/j.gca.2005.05.010
1055   79. Médard, E., McCammon, C. A., Barr, J. A., & Grove, T. L. (2008). Oxygen fugacity, temperature
1056   reproducibility, and H2O contents of nominally anhydrous piston-cylinder experiments using graphite
1057   capsules. American Mineralogist, 93(11–12), 1838–1844. https://doi.org/10.2138/am.2008.2842
1058   80. Mercier, J.-C.C., (1972). Structure des péridotites en enclaves dans quelques basaltes d'Europe et
1059   d'Hawaii.vRegards sur la constitution du manteau supérieur. Thèse 3e cycle, Nantes, France, 229 p.
1060   81. Mercier, J. C. C., & Nicolas, A. (1975). Textures and fabrics of upper-mantle peridotites as illustrated
1061   by   xenoliths   from   basalts.   Journal   of   Petrology,   16(1),   454–487.
1062   https://doi.org/10.1093/petrology/16.1.454
1063   82. Mibe, K., Fujii, T., Yasuda, A., (1998). Connectivity of aqueous fluid in the Earth's upper mantle. Geo.
1064   Res. Lett. 25, 1233–1236
1065   83. Mibe, K., Fujii, T., Yasuda, A., 1999. Control of the location of the volcanic front in island arcs by
1066   aqueous fluid connectivity in the mantle wedge. Nature 401, 259–262. https://doi.org/10.1038/45762
1067   84. Mighani, S., Wang, H., Shuster, D. L., Borlina, C. S., Nichols, C. I. O., & Weiss, B. P. (2020). The end
1068   of the lunar dynamo. Science, 1–8.
1069   85. Minarik, W.G., Watson, E.B., (1995). Interconnectivity of carbonate melt at low melt fraction. Earth.
1070   Planet. Sci. Lett 133(3–4):423–437. https://doi.org/10.1016/0012-821X(95)00085
1071   86. Monteux, J., Jellinek, A. M., & Johnson, C. L. (2011). Why might planets and moons have early
1072   dynamos?   Earth   and   Planetary   Science   Letters,   310(3–4),   349–359.
1073   https://doi.org/10.1016/j.epsl.2011.08.014

1074   87.   Monteux, J., Arkani-Hamed, J., (2014). Consequences of giant impacts in early Mars: Core merging and
1075   Martian dynamo evolution. J. Geophys. Res. 119, 480–505.

1076   88.   Monteux, J., Andrault, D., & Samuel, H. (2016). On the cooling of a deep terrestrial magma ocean.
1077   Earth and Planetary Science Letters, 448, 140–149. https://doi.org/10.1016/j.epsl.2016.05.010

1078   89.   Monteux J., Andrault D., Guitreau M., Samuel H., Demouchy S. (2020). A mushy Earth's mantle for
1079   more than 500 Myr after the magma ocean solidification. Geophysical Journal International
1080   DOI:10.1093/gji/ggaa064

1081   90.   Namur, O., Collinet, M., Charlier, B., Grove, T. L., Holtz, F., & McCammon, C. (2016). Melting
1082   processes and mantle sources of lavas on Mercury. Earth and Planetary Science Letters, 439, 117–128.
1083   https://doi.org/10.1016/j.epsl.2016.01.030

1084   91.   Neuville, D. R., Courtial, P., Dingwell, D. B., & Richet, P. (1993). Thermodynamic and rheological
1085   properties of silicate melts. Contributions to Mineralogy and Petrology, 113, 572–581.

1086   92.   Ni, H., Keppler, H., & Behrens, H. (2011). Electrical conductivity of hydrous basaltic melts:
1087   Implications for partial melting in the upper mantle. Contributions to Mineralogy and Petrology, 162(3),
1088   637–650. https://doi.org/10.1007/s00410-011-0617-4

1089   93.   Ni, H., Hui H., & G. Steinle-Neumann (2015). Transport properties of silicate melts. Rev. Geophys.,
1090   53, 715–744, doi:10.1002/2015RG000485.

1091   94.   Nimmo, F. (2002). Why does Venus lack a magnetic field? Geology, 30(11), 987–990.
1092   https://doi.org/10.1130/0091-7613(2002)030<0987:WDVLAM>2.0.CO;2

1093   95.   Novella, D., Frost, D.J., Hauri, E.H., Bureau, H., Raepsaet, C., Roberge, M., (2014). The distribution of
1094   H2O between silicate melt and nominally anhydrous peridotite and the onset of hydrous melting in the
1095   deep upper mantle. Earth Planet Sci Lett 400:1–13. https ://doi. org/10.1016/j.epsl.2014.05.006.

1096   96.   O'Rourke, J. G., Buz, J., Fu, R. R., & Lillis, R. J. (2019). Detectability of Remanent Magnetism in the
1097   Crust   of   Venus.   Geophysical   Research   Letters,   46(11),   5768–5777.
1098   https://doi.org/10.1029/2019GL082725

1099   97.   Pertermann, M., & Hofmeister, A. M. (2006). Thermal diffusivity of olivine-group minerals at high
1100   temperature. American Mineralogist, 91, 1747–1760.

1101   98.   Picard, D., Arbaret, L., Pichavant, M., Champallier, R., & Launeau, P. (2013). The rheological transition
1102   in plagioclase-bearing magmas. Journal of Geophysical Research: Solid Earth, 118(4), 1363-1377.

1103   99.   Pommier, A., Leinenweber, K., & Tran, T. (2019). Mercury ' s thermal evolution controlled by an
1104   insulating   liquid   outermost   core ?   Earth   and   Planetary   Science   Letters,   517,   125–134.
1105   https://doi.org/10.1016/j.epsl.2019.04.022

1106   100.   Richet, P., & Fiquet, G. (1991). High-temperature heat capacity and premelting of minerals in the system
1107   MgO-CaO-Al2O3-SiO2.   Journal   of   Geophysical   Research,   96(B1),   445–456.
1108   https://doi.org/10.1029/90JB02172

1109   101.   Romine, W. L., Whittington, A. G., Nabelek, P. I., & Hofmeister, A. M. (2012). Thermal diffusivity of
1110   rhyolitic glasses and melts: Effects of temperature, crystals and dissolved water. Bulletin of
1111   Volcanology, 74(10), 2273–2287. https://doi.org/10.1007/s00445-012-0661-6

1112   102.   Sakamaki, T., Suzuki, A., & Ohtani, E. (2006). Stability of hydrous melt at the base of the Earth's upper
1113   mantle. Nature, 439(7073), 192–194. https://doi.org/10.1038/nature04352

1114   103.   Sambridge, M., Mosegaard, K., (2002). Monte Carlo methods in geophysical inverse problems. Reviews
1115   of Geophysics, 40(3), 3-1.

1116   104.   Schiavi, F., Bolfan-Casanova, N., Withers, A. C., Médard, E., Laumonier, M., Laporte, D., et al. (2018).
1117   Water quantification in silicate glasses by Raman spectroscopy: Correcting for the effects of confocality,
1118   density   and   ferric   iron.   Chemical   Geology,   483(February),   312–331.
1119   https://doi.org/10.1016/j.chemgeo.2018.02.036

1120 105. Schmeling, H., (1986). Numerical models on the influence of partial melton elastic, anelastic and
1121   electrical properties of rocks. Part II: electrical conductivity. Phys. Earth Planet. Inter. 43(2):123–136.
1122   https://doi.org/10.1016/0031-9201(86)90080 -4.

1123 106. Schubert, G., Chan, K. H., Liao, X., & Zhang, K. (2004). Planetary dynamos: Effects of electrically
1124   conducting flows overlying turbulent regions of magnetic field generation. Icarus, 172(2), 305–315.
1125   https://doi.org/10.1016/j.icarus.2004.06.007

1126 107. Shea, T., Houghton, B.F., Gurioli, L., Cashman, K.V., Hammer, J.E., Hobden, B.J., (2010). Textural
1127   studies of vesicles in volcanic rocks: an integrated methodology. J. Volcanol. Geotherm. Res; 190(3–
1128   4):271–289. https ://doi.org/10.1016/j.jvolg eores .2009.12.003

1129 108. Smith, D. S., Fayette, S., Grandjean, S., Martin, C., Telle, R., & Tonnessen, T. (2003). Thermal
1130   resistance of grain boundaries in alumina ceramics and refractories. Journal of the American Ceramic
1131   Society, 86(1), 105–111. https://doi.org/10.1111/j.1151-2916.2003.tb03285.x

1132 109. Smith, D. S., Alzina, A., Bourret, J., Nait-Ali, B., Pennec, F., Tessier-Doyen, N., Otsu, .K, Matsubara,
1133   H., Elser, P., & Gonzenbach, U. T. (2013).Thermal conductivity of porous materials. J. Mater. Res., 28
1134   (17).

1135 110. Solomatov, V., (2007). Magma Oceans and Primordial Mantle Differentiation. Schubert, G. (Ed.),
1136   Treatise of Geophysics, vol.9. Elsevier.

1137 111. Spera, F., J., (2000). Physical properties of magma. Encyclopedia on Volcanoes

1138 112. Stanley, S., Bloxham, J., Hutchison, W. E., & Zuber, M. T. (2005). Thin shell dynamo models consistent
1139   with Mercury's weak observed magnetic field. Earth and Planetary Science Letters, 234(1–2), 27–38.
1140   https://doi.org/10.1016/j.epsl.2005.02.040

1141 113. Stevenson, D. J., Spohn, T., & Schubert, G. (1983). Magnetism and thermal evolution of the terrestrial
1142   planets. Icarus, 54(3), 466–489. https://doi.org/10.1016/0019-1035(83)90241-5.

1143 114. Stevenson, D. J. (1987). Mercury's magnetic field: A thermoelectric dynamo? Earth and Planetary
1144   Science Letters, 82(1–2), 114–120. https://doi.org/10.1016/0012 821X(87)90111-7.

1145 115. Strom, R. G., & Sprague, A. L. (2003). Exploring Mercury: the iron planet. Springer Science & Business
1146   Media.

1147 116. Tarduno, J.A., Cottrell, R.D., Watkeys, M.K., Hofmann, A., Doubrovine, P.V., Mamajek, E.E., Liu, D.,
1148   Sibeck, D.G., Neukirch, L.P. and Usui, Y., (2010). Geodynamo, solar wind, and magnetopause 3.4 to
1149   3.45 billion years ago. science, 327(5970), pp.1238-1240.

1150 117. Tian, Z., Zuber, M. T., & Stanley, S. (2015). Magnetic field modeling for Mercury using dynamo models
1151   with a stable layer and laterally variable heat flux. Icarus, 260, 263–268.
1152   https://doi.org/10.1016/j.icarus.2015.07.019.

1153 118. Tikoo, S. M., Weiss, B. P., Cassata, W. S., Shuster, D. L., Gattacceca, J. Ô., Lima, E. A., et al. (2014).
1154   Decline of the lunar core dynamo. Earth and Planetary Science Letters, 404, 89–97.
1155   https://doi.org/10.1016/j.epsl.2014.07.010

1156 119. Tyburczy, J. A., & Waff, H. S. (1983). electrical conductivity of molten basalt and andesite to 25 kilobars
1157   pressures: geophysical significance and implications for charge transport and melt structure. Journal of
1158   Geophysical Research, 88(2), 2413–2430.

1159 120. Von Bargen, N., Waff, H.S., (1986). Permeabilities, interfacial areas and curvatures of partially molten
1160   systems: results of numerical computations of equilibrium microstructures. J. Geophys. Res. 91:9261–
1161   9276.

1162 121. Waff, H.S., (1974). Theoretical consideration of electrical conductivity in a partially molten mantle and
1163   implications for geothermometry. J. Geophys. Res. 79(26):4003–4010.

1164 122. Watanabe, H. (1982). Thermochemical properties of synthetic high-pressure compounds relevant to the
1165   Earth's mantle.

1166   123. Watanabe, T., Kurita, K. (1993). The relationship between electrical conductivity and melt fraction in a
1167   partially molten simple system: Archie's law behavior. Physics of the earth and planetary interiors, 78(1-
1168   2), 9-17.
1169   124. Watson, E.B., Brenan, J.M., Baker, D.R., (1991). Continental Mantle. Oxford Univeristy Press.
1170   125. Weidenschilling, S. J. (1978). Iron/silicate fractionation and the origin of Mercury. Icarus, 35(1), 99–
1171   111. https://doi.org/10.1016/0019-1035(78)90064-7
1172   126. Weiss, B. P., Berdal, James, S., Elkins-Tanton, L., Stanley, S., Lima, E. A., & Carporzen, L. (2008).
1173   Magnetism on the Angrite Differentiation of Planetesimals. Scientific Reports, 322(October), 713–716.
1174   127. Wurm, G., Trieloff, M., & Rauer, H. (2013). Photophoretic separation of metals and silicates: The
1175   formation of mercury-like planets and metal depletion in chondrites. Astrophysical Journal, 769(1).
1176   https://doi.org/10.1088/0004-637X/769/1/78
1177   128. Xu, Y., Shankland, T. J., Linhardt, S., Rubie, D. C., Langenhorst, F., & Klasinski, K. (2004). Thermal
1178   diffusivity and conductivity of olivine, wadsleyite and ringwoodite to 20 GPa and 1373 K. Physics of
1179   the Earth and Planetary Interiors, 143(1–2), 321–336. https://doi.org/10.1016/j.pepi.2004.03.005
1180   129. Yoshino, T., Takei, Y., Wark, D.A;, Watson, E.B., (2005). Grain boundary wetness of texturally
1181   equilibrated rocks, with implications for seismic properties of the upper mantle. J. Geophys. Res. B
1182   Solid Earth 110(8):1–16. https ://doi.org/10.1029/2004J B0035 44.
1183   130. Yoshino, T., Nishihara, Y., Karato, S. I, 2007. Complete wetting of olivine grain boundaries by a
1184   hydrous melt near the mantle transition zone. Earth Planet. Sci. Lett. 256, 466–472.
1185   https://doi.org/10.1016/j.epsl.2007.02.002
1186   131. Zebib, A., Schubert, G., Dein, J.L., & Paliwal, R.C. (1983) Character and stability of axisymmetric
1187   thermal convection in spheres and spherical shells. Geophys. Astrophys. Fluid Dyn. 23, 1–42.
1188   132. Baohua, Z., Ge, J., Xiong, Z. & Zhai, S., (2019). Effect of water on the thermal properties of olivine
1189   with implications for lunar internal temperature. J.Geo.Res. Planets, 124 (12), 3469-3481. doi:
1190   10.1029/2019JE006194
1191

1192 **Figure 1**: Schematic cross-section of the high-pressure cell assembly used for Angstrom method with
1193 multi-anvil apparatus. For glass and melt experiments, thermocouples were inserted in alumina tubes
1194 of 0.6 mm diameter and 4.5 mm length in the sample zone.
1195
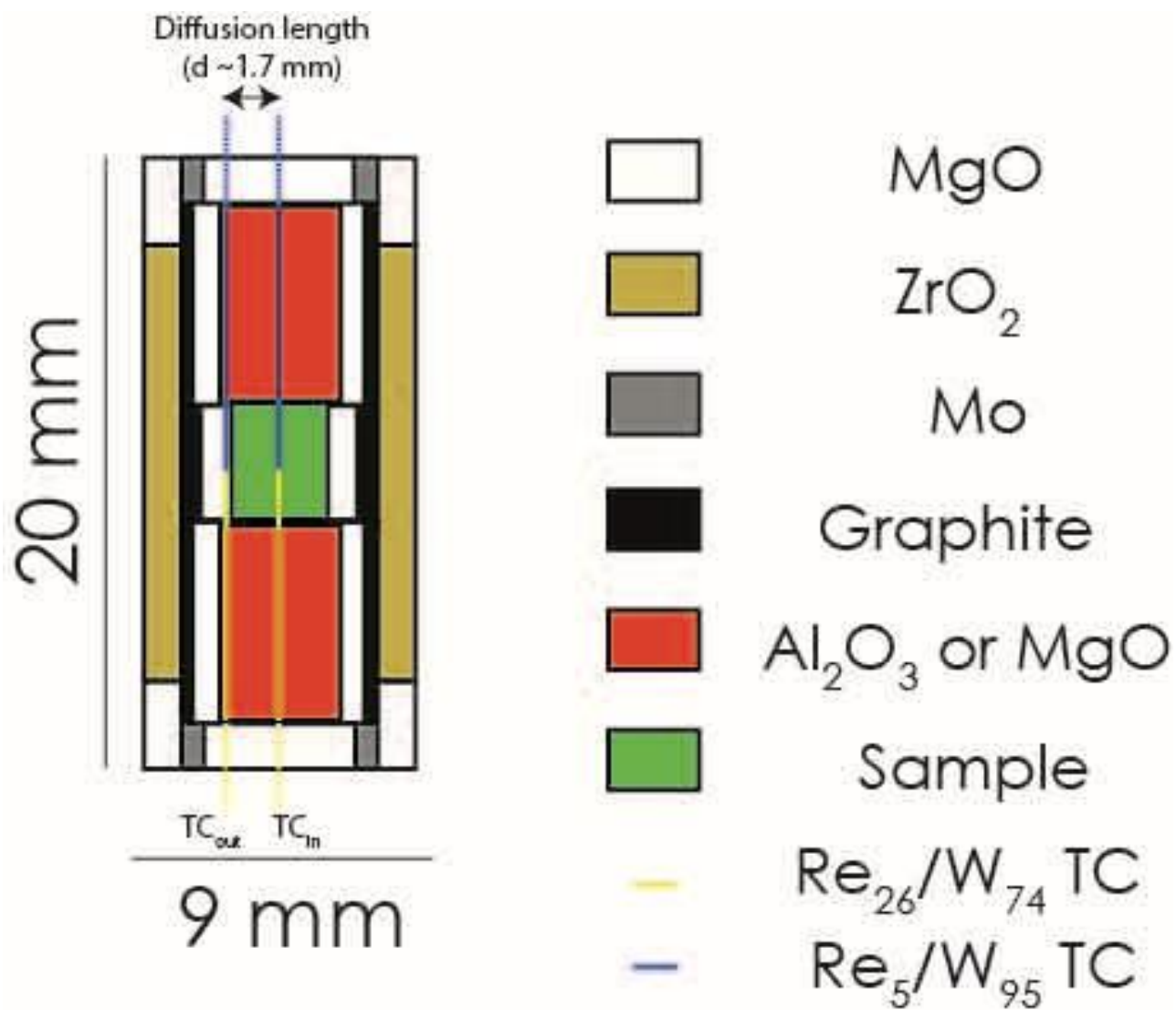
1196
1197
1198
1199
1200
1201
1202
1203
1204
1205
1206
1207
1208
1209

1210 **Figure 2**: Experimental procedure for the measurement of thermal diffusivity of peridotites, glasses
1211 and melts: black, blue and red for cycles 1, 2 and 3 respectively. Heating (H) and cooling (C) parts
1212 of the cycles are separated by black dashed lines (for example H1: 1st cycle heating). The expected
1213 temperatures for sample dehydration (up to ~500°C), glass transition and melting are illustrated in
1214 shaded colors: green, pink and yellow respectively.
1215
1216
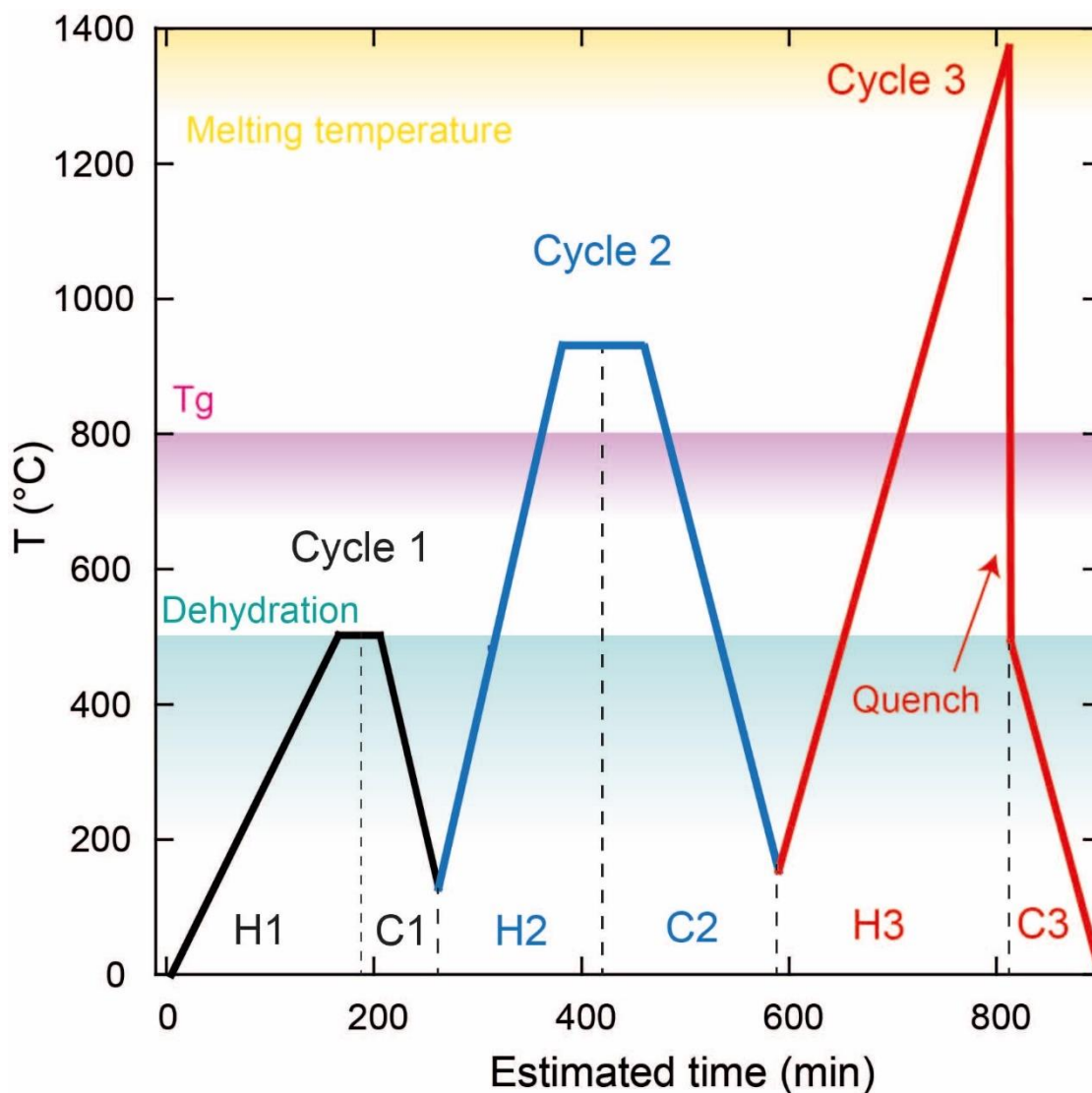
1217
1218
1219

1220 **Figure 3**: Examples of temperature waves recorded at high temperature during M804 experiments.
1221 Such data set is acquired after the sample equilibration at target temperature conditions for a few
1222 minutes (here T = 250°C). Acquisitions are performed at an interval ranging from 40 ms to 200 ms.
1223 At least 10 periods of the temperature oscillation are recorded to ensure a good extraction of phase
1224 shifts and amplitude ratio based on the fitting procedure described in Methods. Upper and lower
1225 frames correspond to temperature measurements performed at frequencies of 0.3 and 1 Hz,
1226 respectively. Red symbols are measured data and the dash thick lines represent the fitted sine waves.
1227

1228
1229
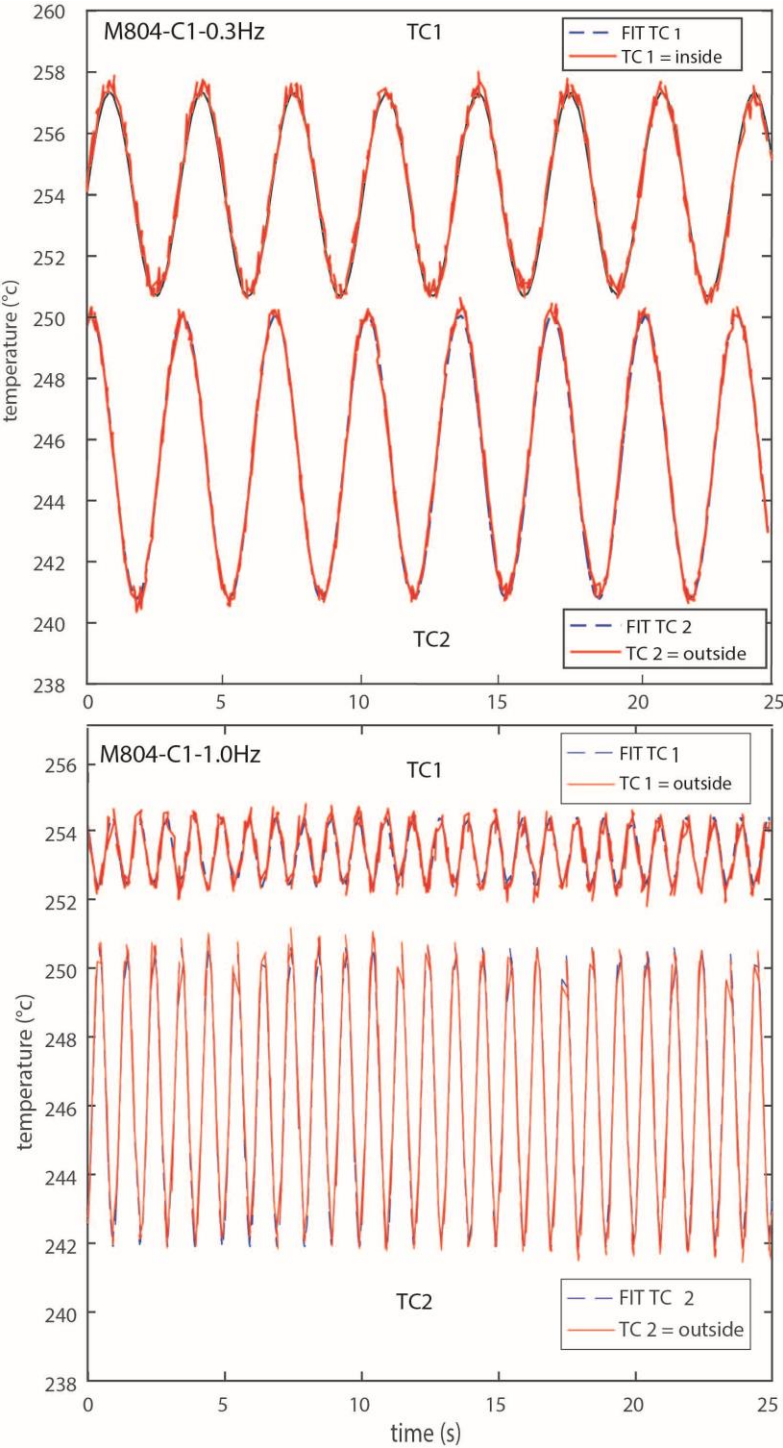
1230 **Figure 4:** Example of refined phase shifts (top panels) and amplitude ratio (bottom panels) as a
1231 function of frequency (from 0.2 to 1.5 Hz, left panels) and temperature (from 428 K to 1191 K, right
1232 panels) for sample M844.
1233

1234
1235
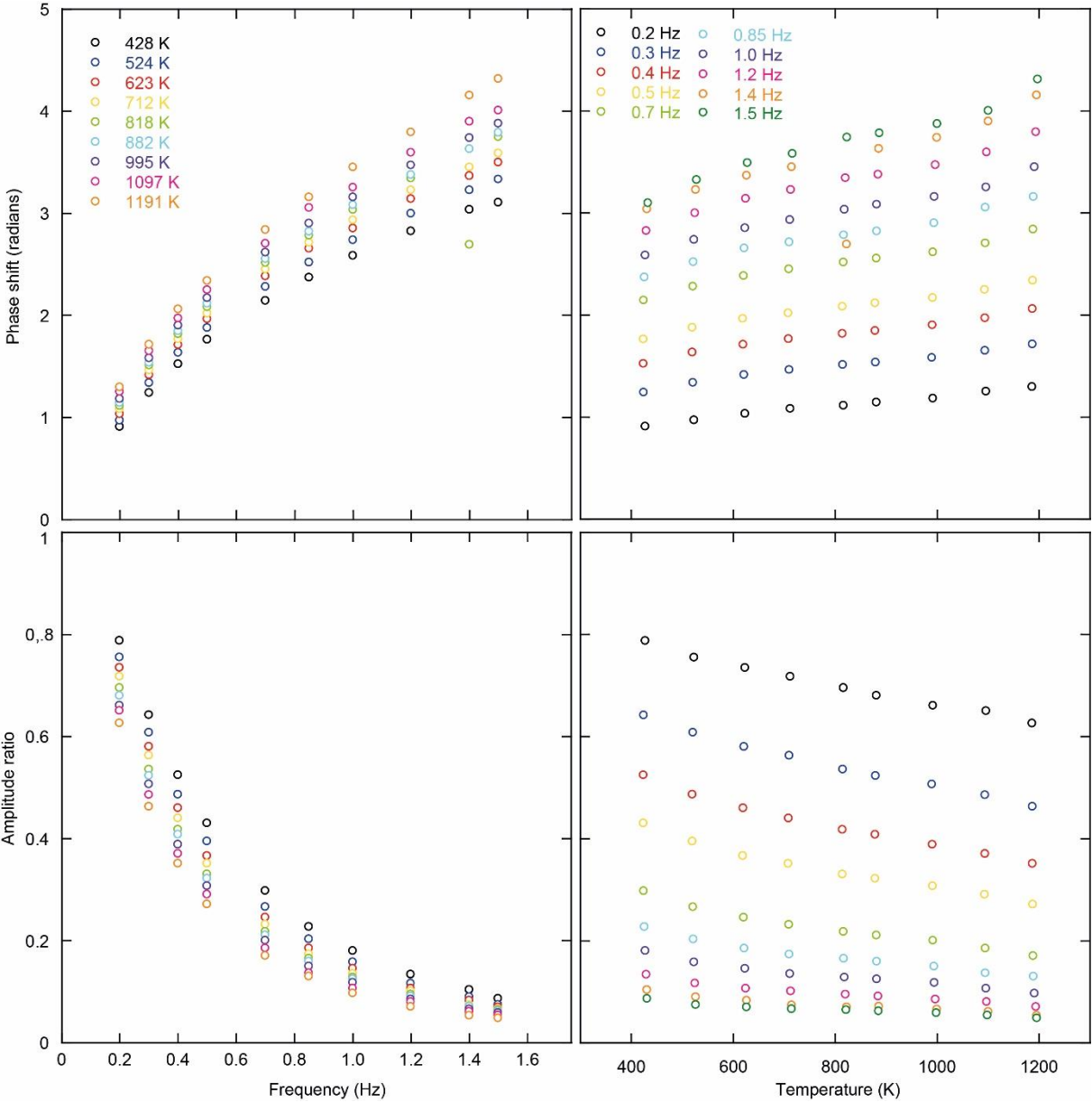
Figure 5: Typical example of a set of raw values of the thermal diffusivity extracted from our measurements for a basaltic glass, presented as a function of the frequency of the heat source. Experimental temperatures range between ~430 and ~1200 K at a pressure of 2GPa (sample M844). Left and right panels correspond to thermal diffusivities calculated from phase shifts and amplitude ratios, respectively. The color code is kept similar in both panels. The fit through the data is made following the equation $D = D_0 + A\ exp\ (-f/f_0)$ (Xu et al., 2004), were D_0 is the high-frequency asymptote of the diffusivity (see text). Error bars are generally within the size of the symbol.
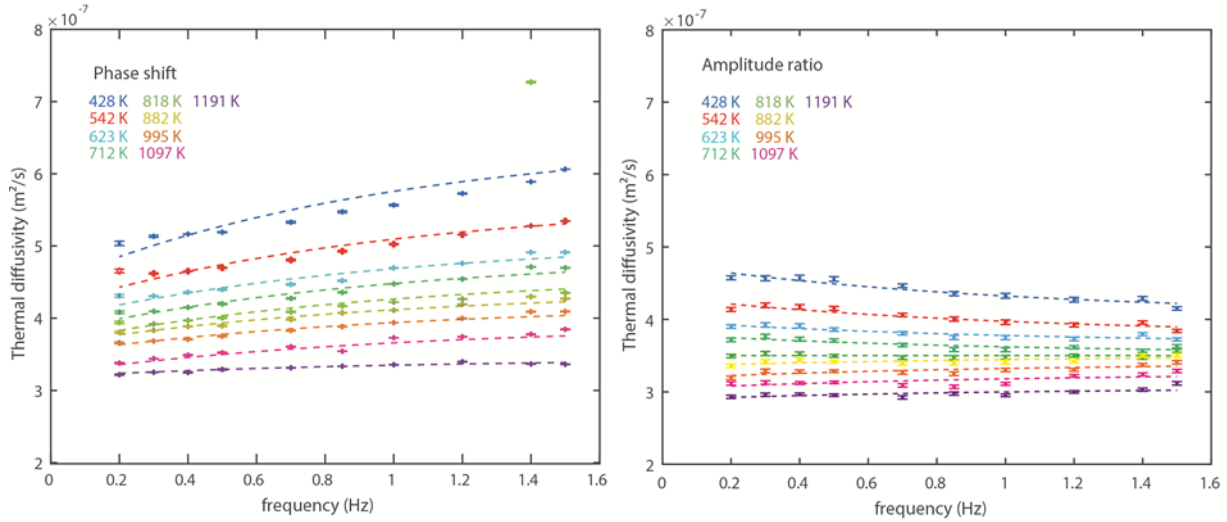
Figure 6: Thermal diffusivities data refined for our peridotites, basalts and rhyolites samples (from
1249   top to bottom) as a function of temperature. Associated fits are represented with a solid line of the
1250   same color than the symbols. Error bars are shown when larger than the symbol size. Several basaltic
1251   (M807, M662) and rhyolite (M848, M808) samples were partially recrystallized during the annealing
1252   and dehydration procedures prior to the conductivity measurement, as indicated by their high
1253   conductivity values at low temperatures. Thermal diffusivities values converge at high temperatures
1254   and melting.
1255
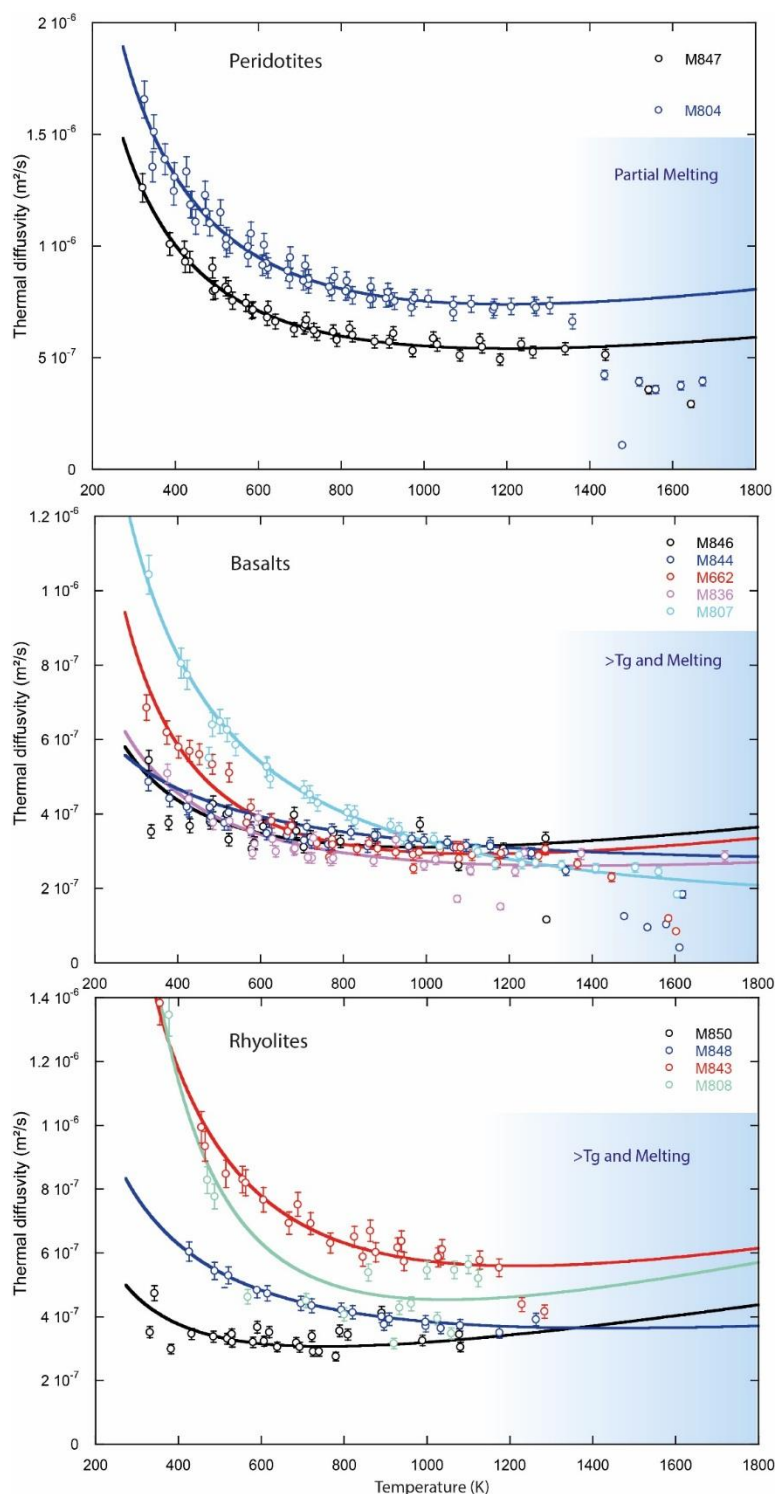
1256

Figure 7: Thermal conductivities inferred from diffusivities (Figure 6), heat capacities and densities
1258 (see Figure S4), based on Eq. 17 of the main text.
1259

1260
1261

33
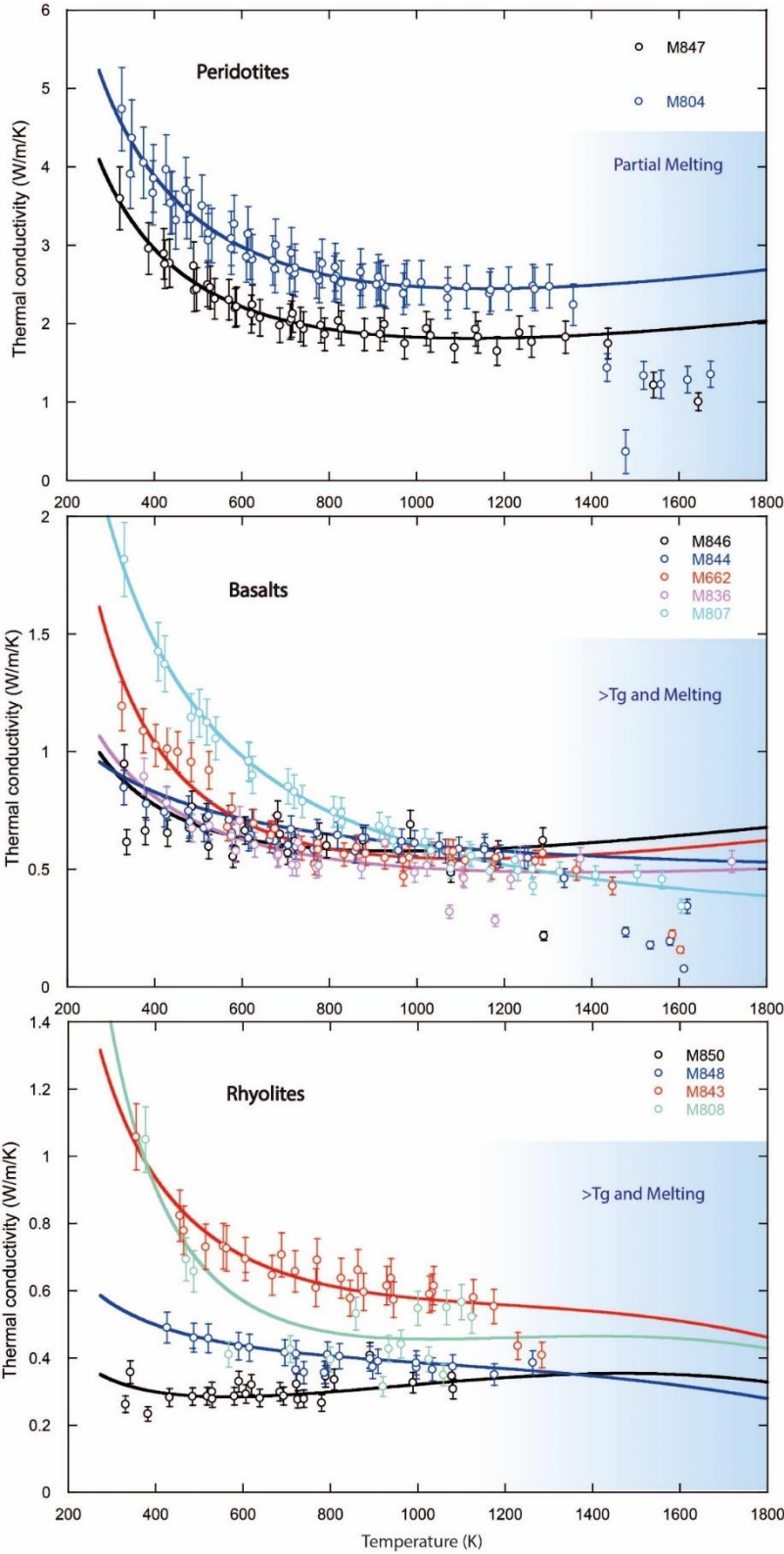
Figure 8: Comparison with the literature of our thermal diffusivities obtained our peridotite (upper panel), basaltic (center panel) and rhyolitic (lower panel) starting materials. Solids (peridotite and glasses) and melts are represented in thick lines and thick dashed line, respectively. Literature data are reported with thinner dashed lines (grey to black). Diopside (Di) glass and melt, XAlSi$_3$O$_8$ glass, Anorthite melt (An), Albite melt (Ab) and orthose melt (FK) from Hofmeister et al. 2009, NCr Rhyolite from Romine et al. 2012 and Enstatite glass from Hofmeister et al. 2014.
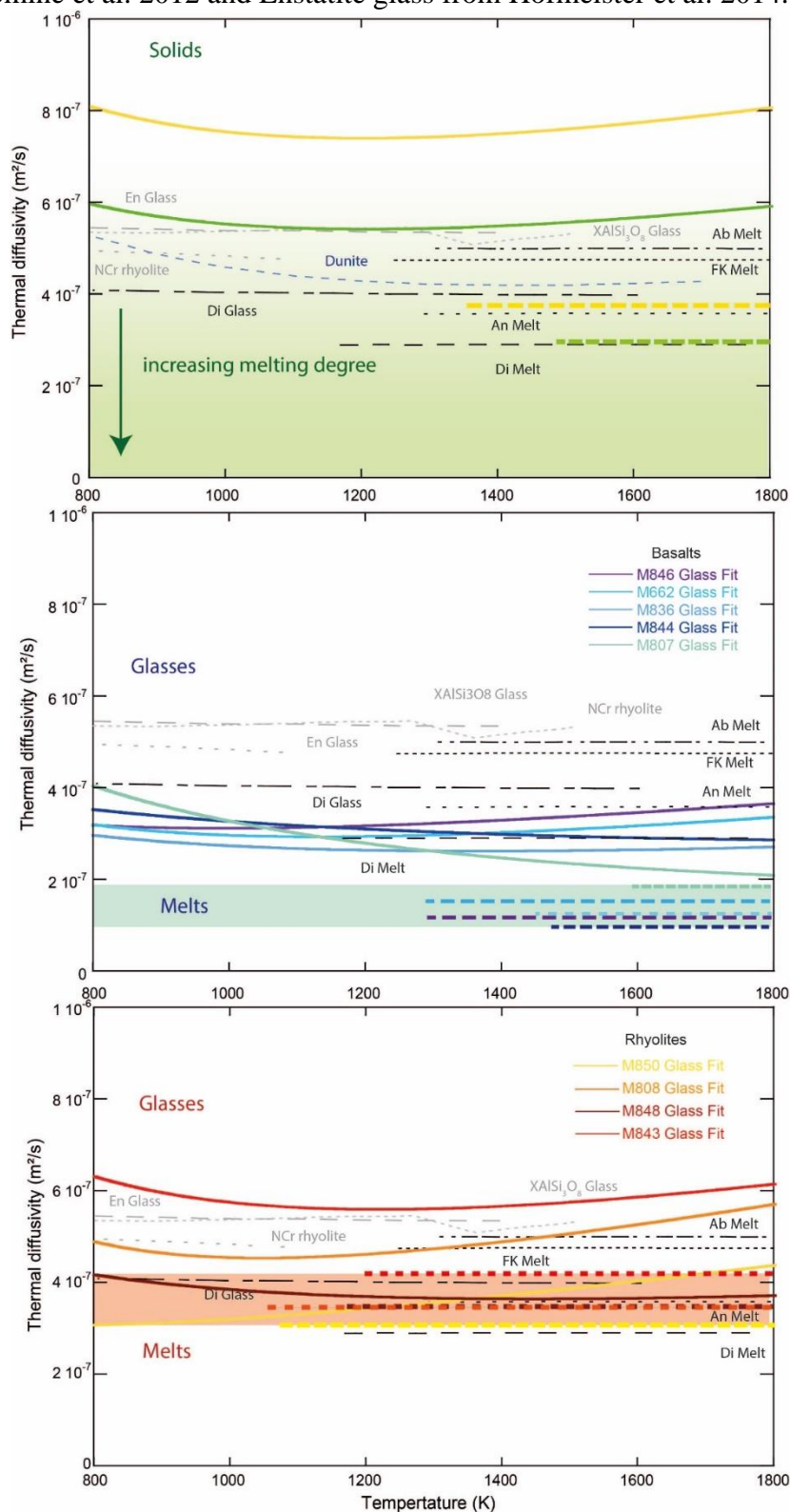
Figure 9: Our best model of the evolution of thermal diffusivity as a function of the melt fraction at high temperature (>1200 K), based on all available data sets. Solid peridotites at low and high temperature are represented with green and blue diamonds, respectively. Partially molten peridotites with 6.4% and 23.3% of melt (see Supplementary Text S3) are represented with red circles and melts (basalts and rhyolites) are represented with blue and pink circles. All the errors represented are 1 standard deviation. The fit represented is using a model of thermal resistors in series (Eq. 22), which fits our data set very well (see Figure S14).
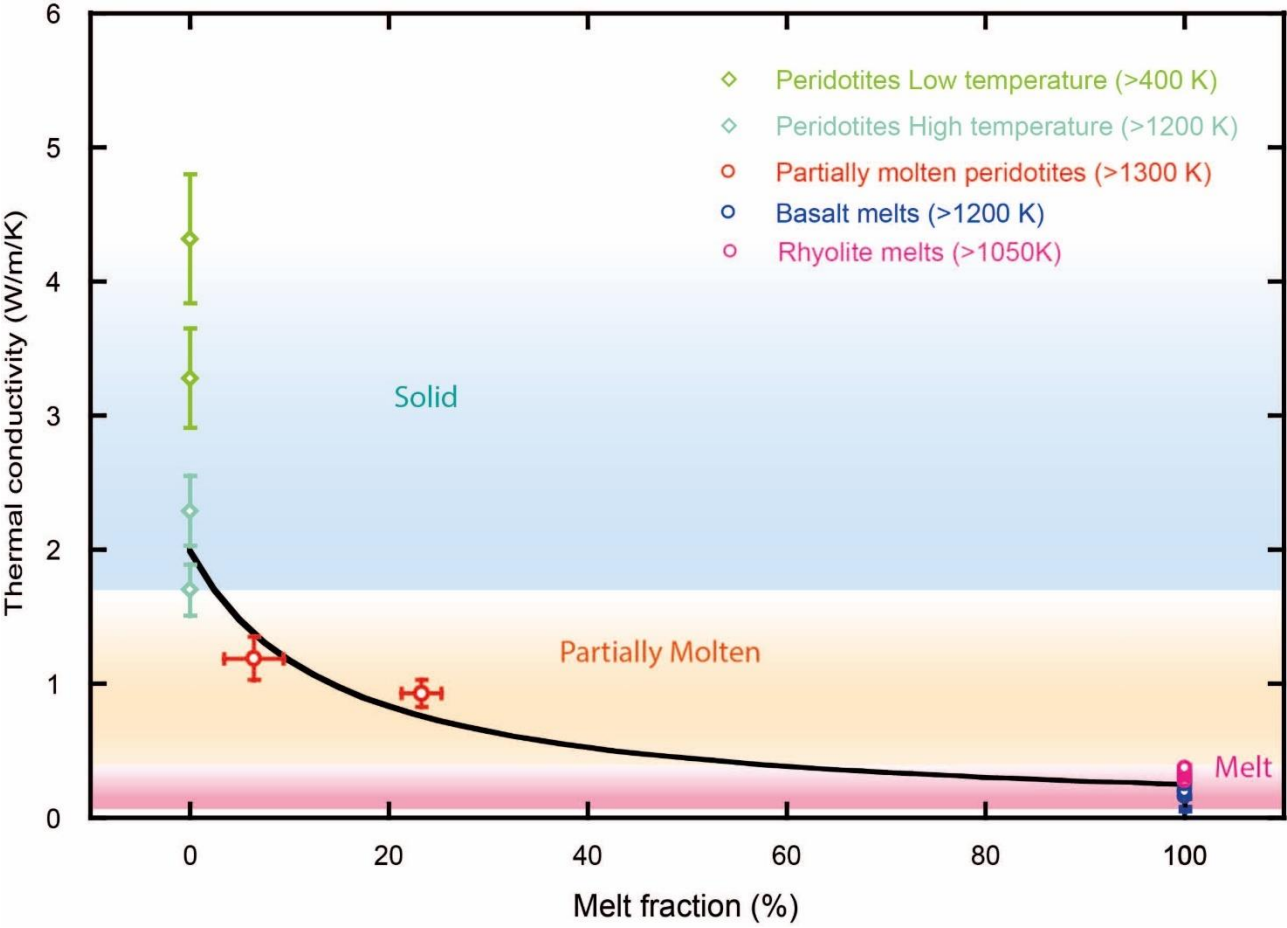
1279 **Figure 10**: Schematic representation of the geometry and of the heat flows computed in our model.
1280
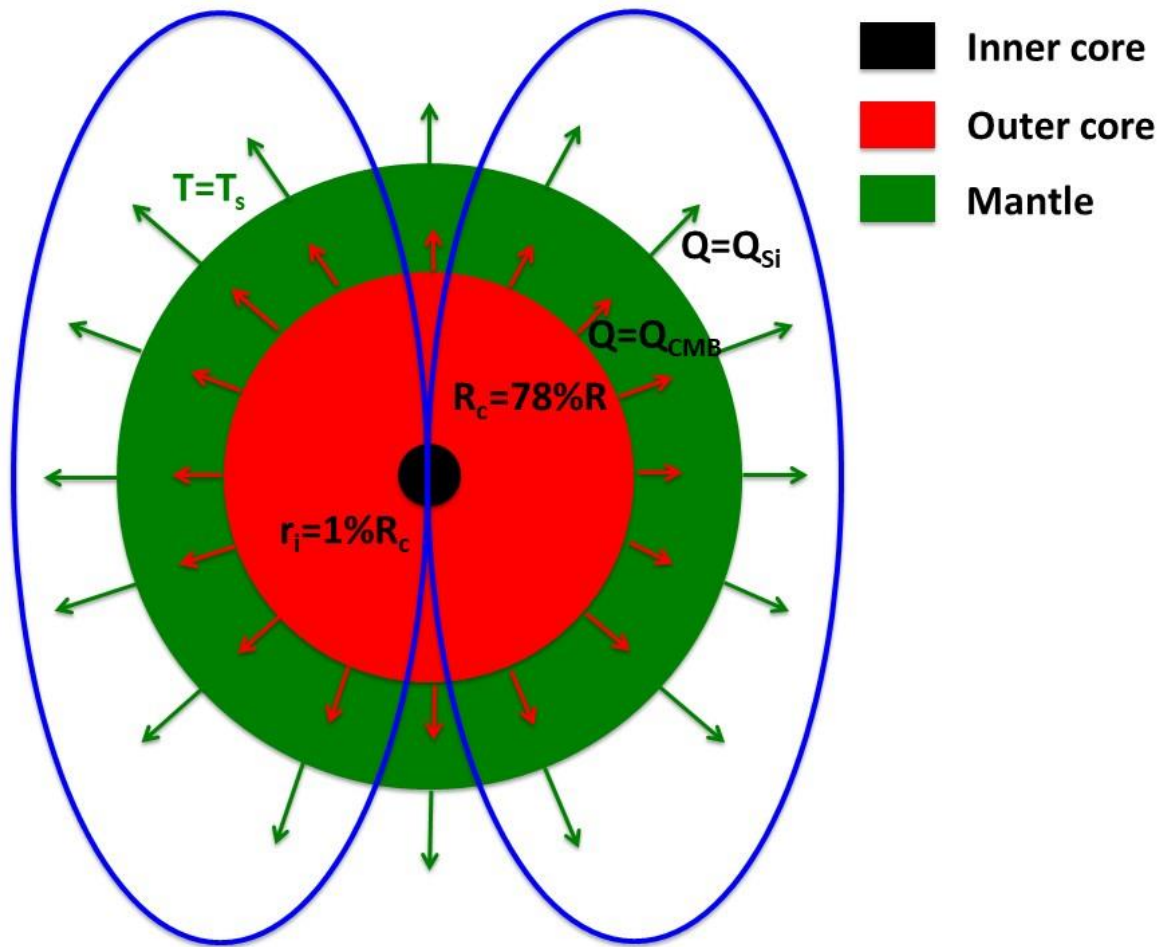
1281

Figure 11: Heat flows as a function of the planetary radius for a fully solid planetary mantle. The
1283   black and grey lines represent the critical heat flow needed for a thermally driven dynamo for $k_c = 40$
1284   and 4 W/m/K, respectively (Conditions 1 and 2, Eq. 31). The dark and light green lines represent the
1285   mantle heat flow in a conductive regime for $\kappa_{Si} = 4.32$ and 1.70 W/m/K, respectively (Eq. 35). Green
1286   triangles represent the critical planet size at which $Ra = Ra_c$, therefore corresponding to the minimum
1287   heat flow at the CMB, for mantle viscosity ranging from 10^{18} to 10^{22} Pa.s. Extrapolated values at R
1288 $= R_{Mercury} = 2440$ km are also represented with green circles for conductive heat transfers and red and
1289   pink squares for convective cases (eq. 36) with mantle viscosities indicated nearby. The red dashed
1290   line represents the critical value for Rem = 100 (Condition 3). At the left side of this line, a dynamo
1291   is unlikely. The likely zone for a planet radius capable of powering a dynamo is represented by the
1292   pink shaded area in case $\kappa_{Si} = 4.32$ W/m/K and $\kappa_{core} = 40$ W/m/K.

1293
1294

1295
1296
1297
1298
1299
1300
1301
1302
1303
1304
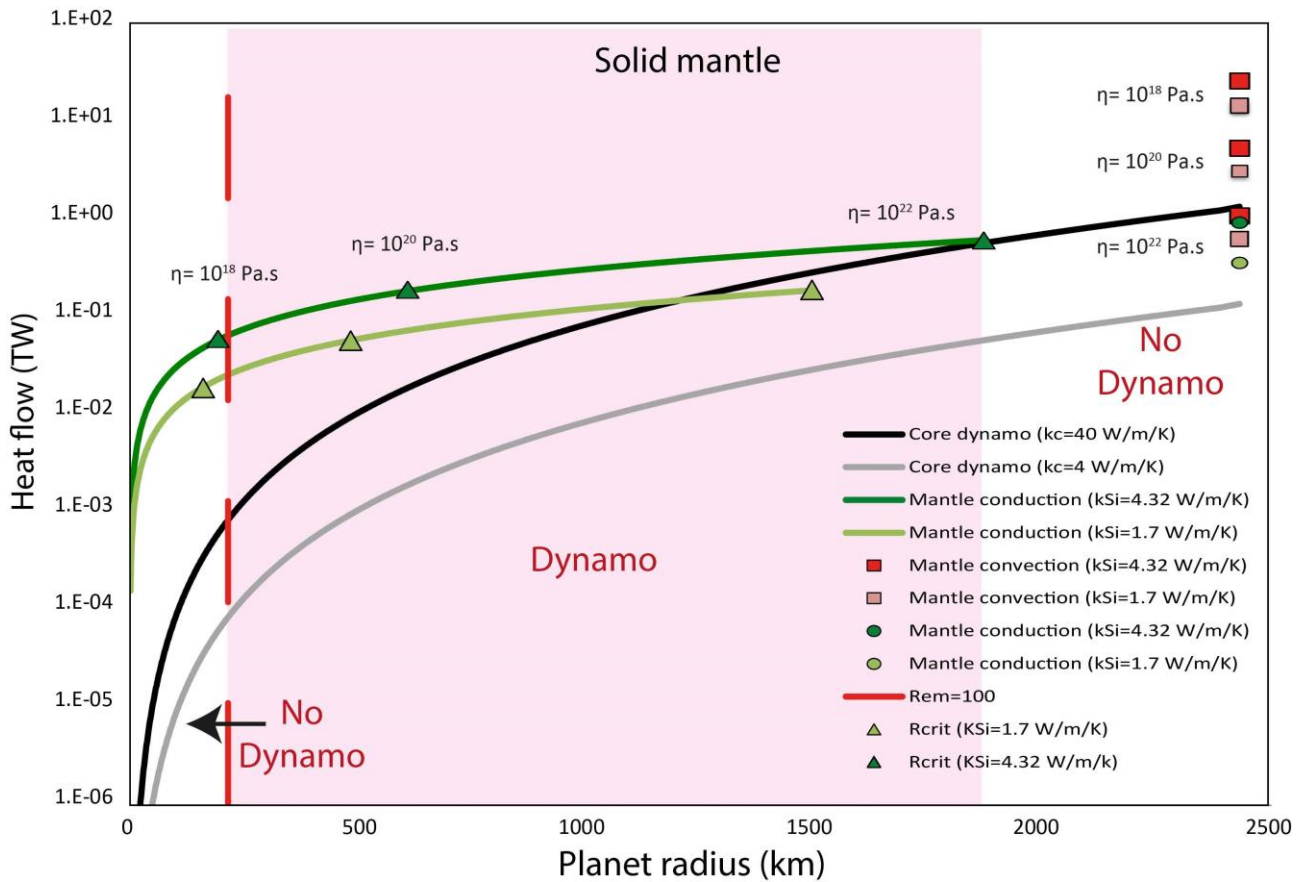
Figure 12.
Heat flows as a function of the planetary radius for a stagnant partially molten planetary mantle. The black and grey lines represent the critical heat flow for a thermally driven dynamo for $k_c = 40$ and 4 W/m/K, respectively (Conditions 1 and 2, Eq. 31). The dark and light green lines represent the mantle heat flow for $\kappa_{Si} = 0.41$ and 0.18 W/m/K, respectively (Eq. 35). Green triangles represent the critical planet size at which $Ra = Ra_c$, for mantle viscosity ranging from 10^{18} to 10^{22} Pa.s. Extrapolated values at $R = R_{Mercury} = 2440$ km are also represented with green circles for conductive heat transfers and red and pink squares for convective cases (Eq. 36) with viscosities indicated nearby. The red dashed line represents the critical value for Rem = 100 (Condition 3). At the left side of this line, a dynamo is unlikely. The likely zone for a planet radius capable of powering a dynamo is represented by the pink shaded area in case $\kappa_{Si} = 0.41$ W/m/K and $\kappa_{core} = 40$ W/m/K.
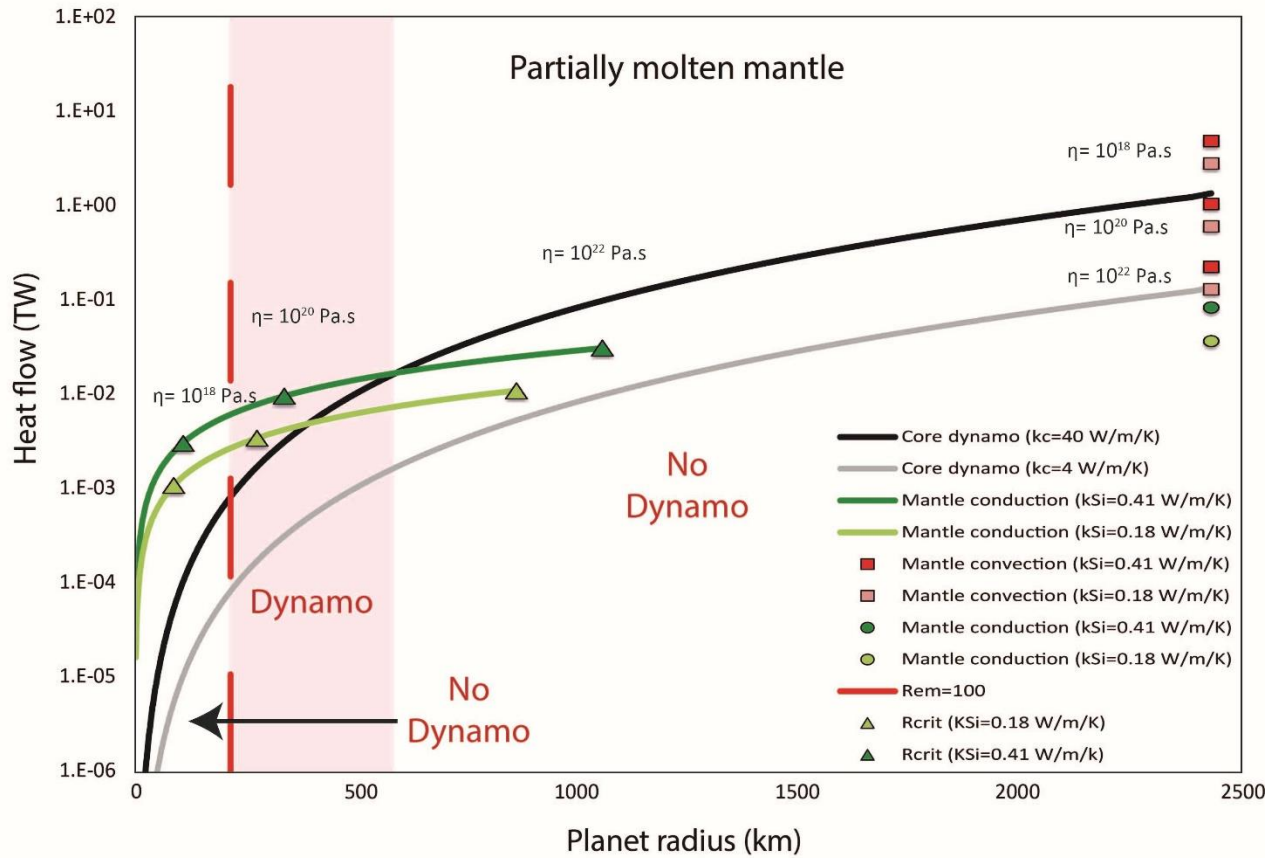
Table 1: Sum up of our Ansgtröm experiments with compositions, P-T ranges and associated parameters.

Run#	M662	M804	M807	M808	M836	M843	M844	M846	M847	M848	M850
Sample name	EPR-MORB	RP4-S2	DR07-S2	GD-S1	Haplo S1	ATHO-S1	DR11-S1	DR11-S2	RP4-S3	ATHO-S2	GD-S2
Composition	MORB	Peridotite	MORB	Rhyolite	haplobasalt	Rhyolite	MORB	MORB	Peridotite	Rhyolite	Rhyolite
Pressure (GPa)	2	2	2	2	2	2	2	2	2	2	2
length before (µm)	1400	1771.2	1061.9	1098.8	1124.6	1541. 9	1141.3	1048.2	1652.9	1045.1	1336.4
length after (µm)	1334.2	1780.0	-	1462.7	1213.2	1666.1	1287.6	1324.9	1643.6	1309.1	1287.4
expected Melting T° (K)	>1600	>1523	>1600	>1173	>1723	>1173	>1600	>1600	>1523	>1173	>1173
Max T (K)	1614	1681	1612	1146	1769	1219	1609	1284	1573	1325	1073
Run duration (min)	544	1089	953	480	832	800	834	439	767	761	610

Table 2: Fitting parameters obtained for the last cycle (C2-H3) of each experiment. Associated errors (1 STD) are given in parenthesis

Run#	a	b	c	R²	R² adj
Peridotites					
M804	7.0e-4 (2.2e-4)	1.06 (0.06)	2.97e-10 (2.8e-11)	0.9659	0.9647
M847	8.8e-4 (7e-4)	1.15 (0.05)	2.37e-10 (1.8e-11)	0.9763	0.9750
Basalts					
M846	8.6e-6 (1.5e-5)	0.5 (0.3)	9.7e-11 (8.4e-11)	0.3933	0.3294
M662	7.2e-4 (1.8e-4)	1.20 (0.04)	1.01e-10 (4.1e-12)	0.9964	0.9962
M836	5.6e-5 (7.6e-5)	0.84 (0.23)	1.03e-10 (3.5e-11)	0.5748	0.5421
M844	1.9e-5 (1.1e-5)	0.63 (0.10)	8.0e-11 (2,3e-11)	0.9608	0.9556
M807	8.1e-4 (1.9e-4)	2.15 (0.04)	4.1e-11 (9e-12)	0.9933	0.9929
Rhyolites					
M850	1.9e-5 (3.5e-5)	0.70 (0.32)	1.7e-10 (7e-11)	0.2788	0.2101
M808	1.8e-2 (7e-2)	1.7 (0.7)	2.3e-10 (1.4e-10)	0.8003	0.7696
M848	1.4e-4 (7e-5)	0.91 (0.09)	1.3e-10 (2.0e-11)	0.9851	0.9826
M843	5.1e-3 (3.3e-3)	1.42 (0.11)	3.18e-10 (3.6e-11)	0.9715	0.9684

1338 **Table 3**: Thermal diffusivities and conductivities retrieved for our samples at low and high
1339 temperatures for solids, above Tg and/or melting temperature (indicated for each group) for melts and
1340 partially molten samples. Literature estimates are also provided on the bottom part: "Xu" refers to
1341 polycrystalline olivine (dunite) measurements performed at ambient pressure (Xu et al., 2004).
1342 "Per06" refers to average values from 3 oriented (100, 010, 001) single crystal measurements at room
1343 pressure (Pertermann and Hofmeister, 2006) and some dunite values are also available in the same
1344 study. "Beck78" refers to Dunite measurements performed at 2 GPa (Beck et al. 1978). Regarding
1345 melts, literature data are taken from Hofmeister et al. (2009), Di: diopside, An : anorthite, Fk : orthose,
1346 Ab : albite. Finally, data from a few rhyolites Ncar, NCr and SCE are selected from Romine et al.
1347 (2012). When literature data are available in the form of thermal diffusivities, their conductivities are
1348 obtained using either the Cp and ρ provided in the source study or from our own parameters if not
1349 available (see Supplementary Materials).

SAMPLE NAME	Temperature range	Melt fraction	STD	κ	STD	D	STD
		%	%	W/m/K	W/m/K	m²/s	m²/s
SOLIDS							
M804	LT < 400K	0	0	4.32	0.48	1.66E-06	2.05E-09
M847	LT < 400K	0	0	3.28	0.37	1.26E-06	3.34E-09
M804	HT >1200 K	0	0	2.29	0.26	7.33E-07	1.80E-09
M847	HT >1200 K	0	0	1.70	0.19	5.39E-07	6.13E-10
Partially molten samples							
M804	>1300 K	6.44	2.98	1.19	0.16	3.74E-07	2.55E-08
M847	>1300 K	23.31	2	0.93	0.10	2.92E-07	1.22E-10
MELTS							
BASALTS	MELT >1200K						
M807	>1224 K	100	0	0.34	0.02	1.84E-07	1.51E-09
M844	>1326 K	100	0	0.18	0.01	9.52E-08	2.96E-11
M662	>1450 K	100	0	0.22	0.16	1.20E-07	8.73E-08
M846	>1200 K	100	0	0.22	0.12	1.16E-07	6.47E-08
M836	1180 K	100	0	0.28	0.02	1.51E-07	6.94E-10
rhyolite	Melt >1000 K						
M850	> 1080 K	100	0	0.31	0.03	3.05E-07	2.42E-08
M808	>1060 K	100	0	0.35	0.03	3.47E-07	5.95E-10
M848	>1260 K	100	0	0.39	0.03	3.91E-07	6.21E-10
M843	> 1280 K	100	0	0.41	0.03	4.16E-07	2.36E-10
literature							
SOLIDS							
Olivine Xu 0 GPa LT	294	0	0	4.15	0.42	4.10E-06	2.05E-07
Olivine Xu 0 GPa HT	1377	0	0	1.95	0.19	5.00E-07	2.50E-08
Olivine Hof 16 AVG	300 K	0	0	6.37	0.64	2.37E-06	4.75E-08
Olivine Hof AVG16	>1500 K	0	0	2.76	0.28	7.01E-07	1.40E-08
Dunite Per 06	300 K	0	0	4.22	0.42	1.57E-06	3.15E-08
Dunite 2 Per 06	300 K	0	0	5.35	0.53	1.99E-06	3.99E-08
Dunite Per 06	>1500 K	0	0	1.65	0.17	4.20E-07	8.40E-09
Dunite 2 Per 06	>1500 K	0	0	2.23	0.22	5.65E-07	1.13E-08
Dunite Beck 78 2Gpa	300 K	0	0	4.15	0.42		
Dunite Beck 78 2Gpa	300 K	0	0	5.49	0.55		
Dunite 2 GPa Dry Z19	300 K	0	0	5.21	0.26	1.71E-06	8.55E-08
Dunite 2 GPa 0.08% wt H_2O Z19	300 K	0	0	4.86	0.24	1.59E-06	7.95E-08
Melts							
Di Hof 09	>1140 K	100	0	1.25	0.13	2.89E-07	5.79E-09
An Hof 09	>1290 K	100	0	1.45	0.15	3.58E-07	7.16E-09
Fk Hof 09	>1245 K	100	0	1.45	0.15	4.75E-07	9.50E-09
Ab Hof 09	>1300 K	100	0	1.60	0.16	4.99E-07	9.99E-09
Rhyolite/obsidian							
Ncar Ro 12	1384	100	0	1.53	0.15	5.17E-07	1.03E-08
NCr Ro 12	1365	100	0	1.50	0.15	5.08E-07	1.02E-08
SCE Ro 12	1464	100	0	1.59	0.16	5.31E-07	1.06E-08

1350

1351   **Table 4**: Typical parameter values for heat fluxes calculations displayed in Figures 11 and 12.

1352

κ_c	Core thermal conductivity	4-40	W m^{-1} K^{-1}
α_c	Core thermal expansion	7.7x10^{-5}	K^{-1}
$C_{p,c}$	Core heat capacity	800	J kg^{-1} K^{-1}
υ_c	Core magnetic diffusivity	2	m^2 s^{-1}
μ_c	Core magnetic permeability	4π 10^{-7}	H m^{-1}
ρ_c	Core density	7500	kg m^{-3}
B	Average magnetic field strength	Eq. 3	T
R	Planet radius		m
R_c	Core radius	77% R	m
r_i	Inner core radius	1% R$_c$	m
G	Gravitational constant	6.67x10^{-11}	m^3 kg^{-1} s^{-2}
κ_{Si}	Silicates thermal conductivity	4.32-1.70	W m^{-1} K^{-1}
κ_{Si}	Molten silicates thermal conductivity	0.18-0.41	W m^{-1} K^{-1}
α_{Si}	Silicates thermal expansion	1x10^{-5}	K^{-1}
$C_{p,Si}$	Silicates heat capacity	1000	J kg^{-1} K^{-1}
T_s	Surface temperature	500	K
δ_{Si}	Mantle thickness	33% R	m

1353
1354

Figure 1   Click here to download Figure Fig_1_mod.pdf ⤓

Diffusion length
(d)

MgO

ZrO$_2$

Mo

Graphite

Al$_2$O$_3$ or MgO

Sample

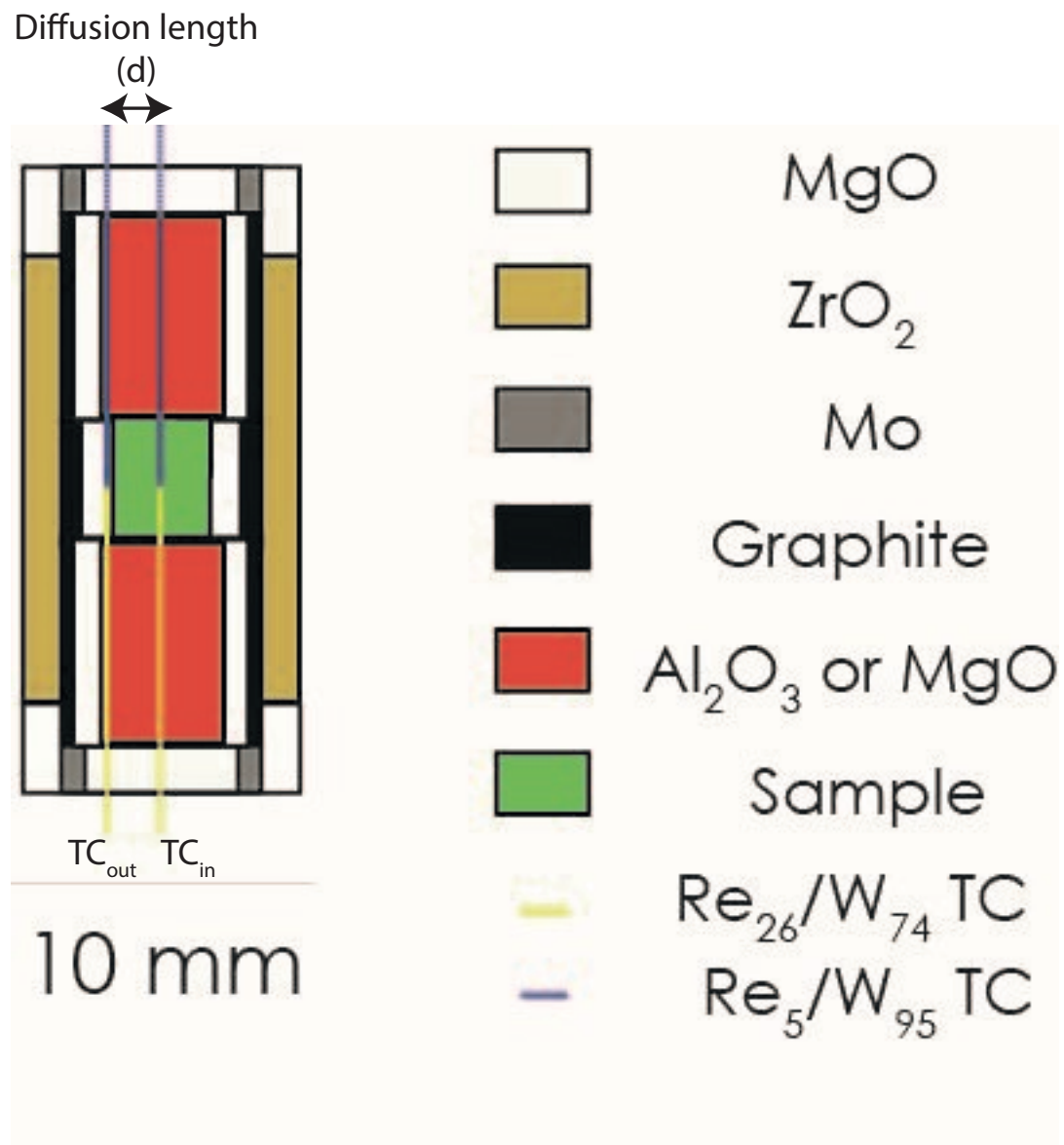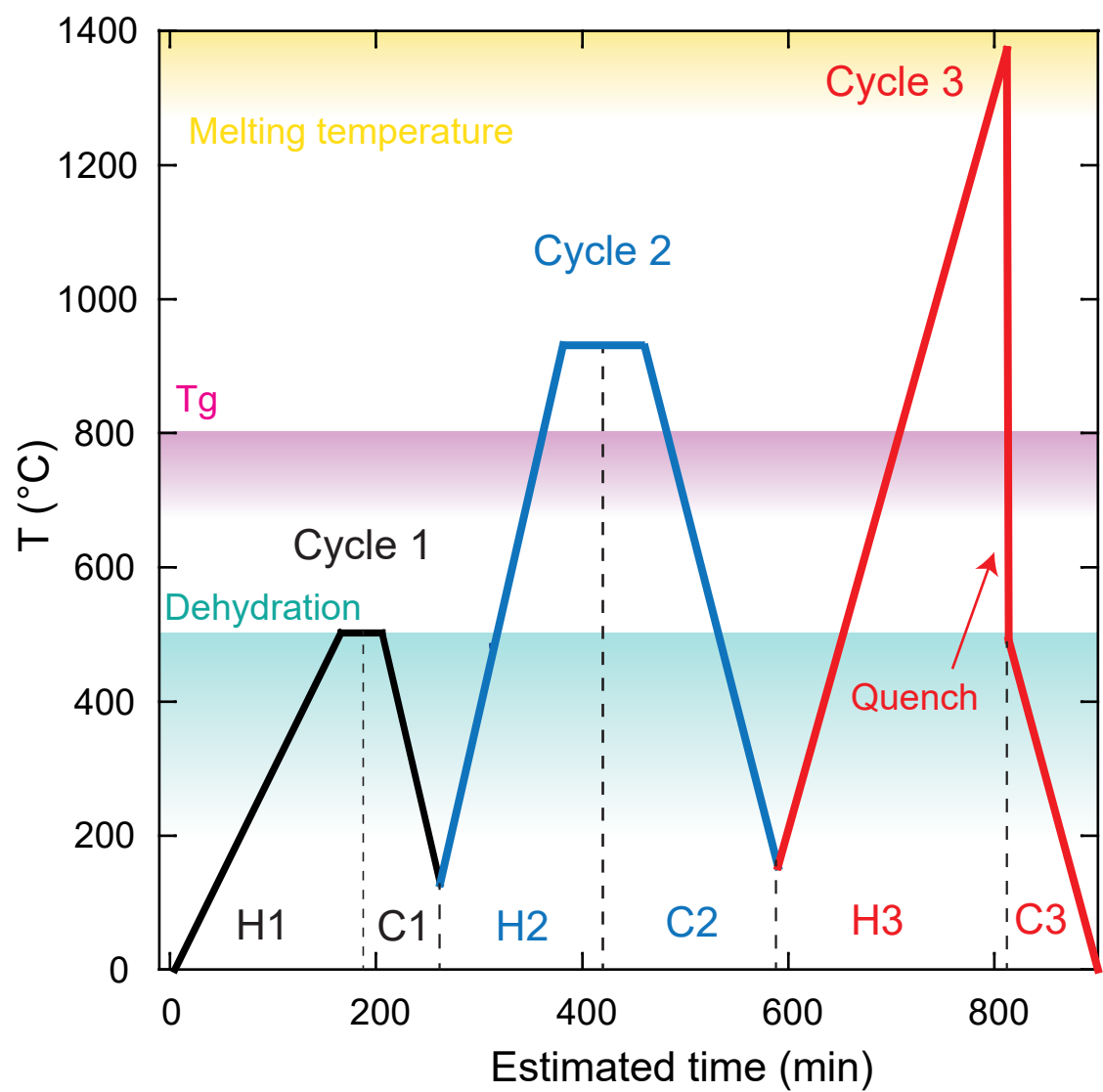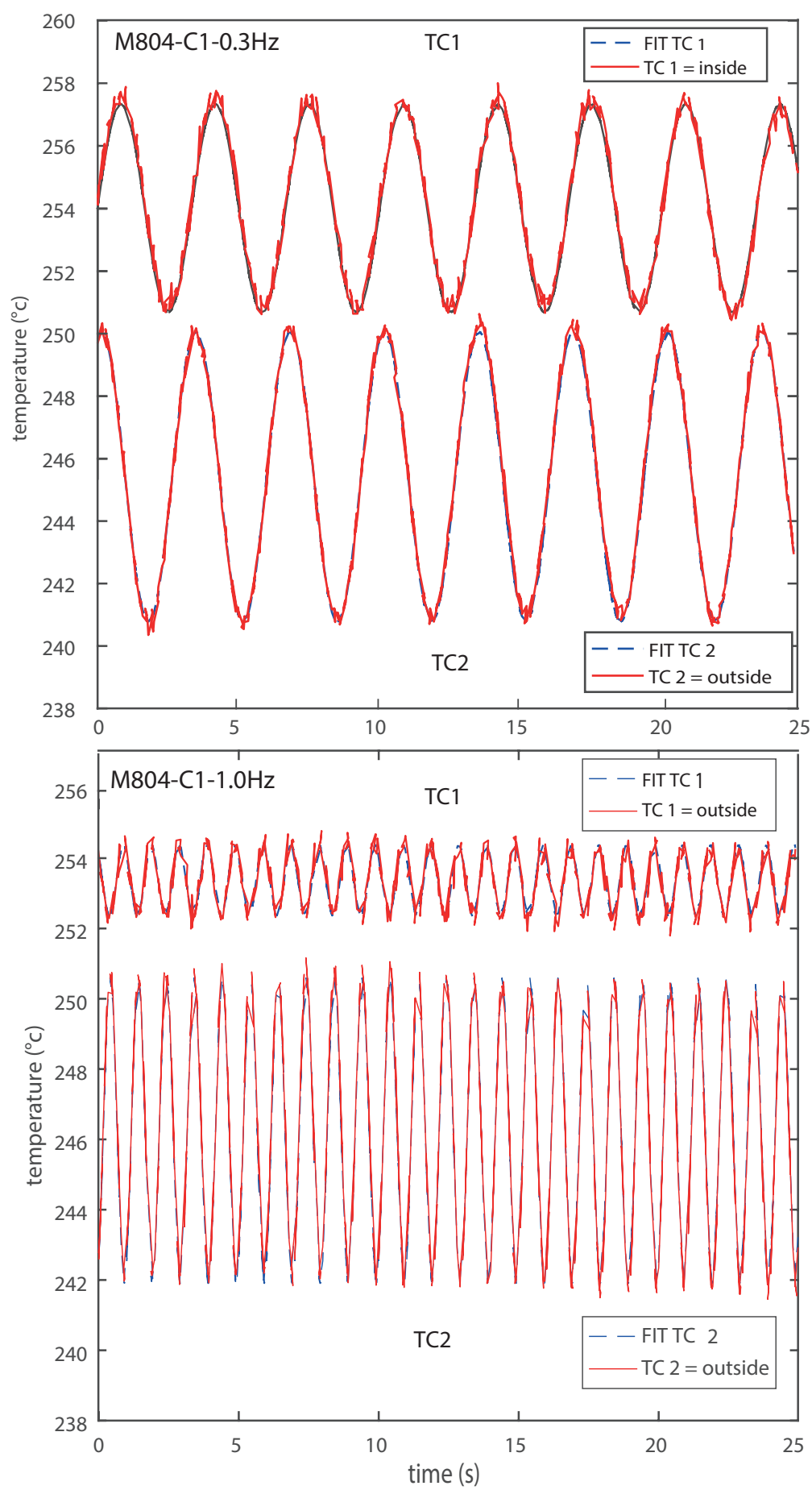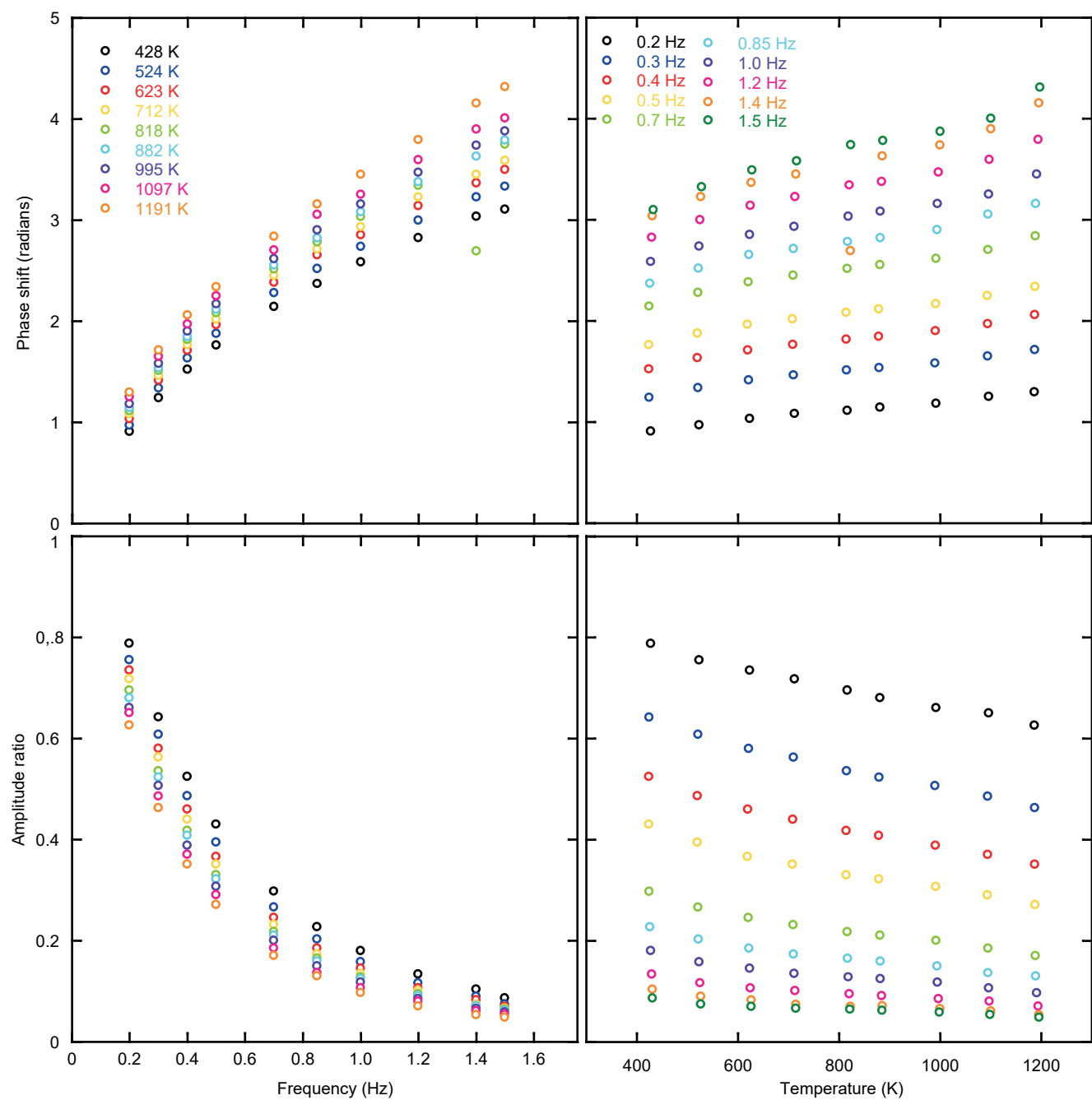Re$_{26}$/W$_{74}$ TC

Re$_5$/W$_{95}$ TC

TC$_{out}$ TC$_{in}$

10 mm

Figure 2

Figure 2

Figure 3

Figure 4

Figure 5

Figure 6

Figure 6

Figure 7

Figure 8

Click here to download Figure Fig_8.pdf ⬇

Figure 9

Figure 10

Figure 11

Figure 11

Figure 12